



Generalized parametric resonance in electrostatically actuated microelectromechanical oscillators

Jeffrey F. Rhoads^{a,*}, Steven W. Shaw^a, Kimberly L. Turner^b, Jeff Moehlis^b,
Barry E. DeMartini^b, Wenhua Zhang^b

^a*Department of Mechanical Engineering, Michigan State University, East Lansing, MI 48824, USA*

^b*Department of Mechanical Engineering, University of California - Santa Barbara, Santa Barbara, CA 93106, USA*

Received 8 June 2005; received in revised form 28 February 2006; accepted 8 March 2006

Available online 23 May 2006

Abstract

This paper investigates the dynamic response of a class of electrostatically driven microelectromechanical (MEM) oscillators. The particular systems of interest are those which feature parametric excitation that arises from forces produced by fluctuating voltages applied across comb drives. These systems are known to exhibit a wide range of behaviors, some of which have escaped explanation or prediction. In this paper we examine a general governing equation of motion for these systems and use it to provide a complete description of the dynamic response and its dependence on the system parameters. The defining feature of this equation is that both the linear and cubic terms feature parametric excitation which, in comparison to the case of purely linear parametric excitation (e.g. the Mathieu equation), significantly complicates the system's dynamics. One consequence is that an effective nonlinearity for the overall system cannot be defined. Instead, the system features separate effective nonlinearities for each branch of its nontrivial response. As such, it can exhibit not only hardening and softening nonlinearities, but also mixed nonlinearities, wherein the response branches in the system's frequency response bend toward or away from one another near resonance. This paper includes some brief background information on the equation of motion under consideration, an outline of the analytical techniques used to reach the aforementioned results, stability results for the responses in question, a numerical example, explored using simulation, of a MEM oscillator which features this nonlinear behavior, and preliminary experimental results, taken from an actual MEM device, which show evidence of the analytically predicted behavior. Practical issues pertaining to the design of parametrically excited MEM devices are also considered.

© 2006 Elsevier Ltd. All rights reserved.

1. Introduction

The recent analysis of parametrically excited microelectromechanical (MEM) oscillators, by the authors and others, has led to the consideration of a certain class of nonlinear equations of motion [1–3]. The defining feature of these equations is that parametric excitation acts on both the linear and cubic terms. As such, the dynamics of these oscillators are quite complex in comparison to a typical Mathieu system, which features

*Corresponding author. Tel.: +1 517 432 1085; fax: +1 517 353 1750.

E-mail address: rhoadsje@msu.edu (J.F. Rhoads).

only linear parametric excitation. One interesting result of this complication is that a single effective nonlinearity for the overall system cannot be defined. Rather, the system features separate effective nonlinearities for each branch of its nontrivial response. Accordingly, the system can exhibit not only the typical hardening and softening nonlinearities, but also mixed nonlinearities wherein the response branches in the system's frequency response bend toward or away from one another near resonance. In fact, such behavior has been observed in experiments, as described subsequently.

The paper begins in Section 2 with a brief description of the types of MEM devices of interest, and a derivation of their governing equation of motion. General analytical results for the undamped system, including information on the existence, stability, and bifurcations of the steady-state solutions, are given in Sections 3 and 4. These results include detailed descriptions of the resulting frequency response curves and the associated phase planes. To facilitate understanding of the aforementioned results, a representative numerical example is explored in Section 5. In Section 6, the effects of light damping on the system are considered. Section 7 explores the given results in the context of a specific MEM oscillator, provides the pertinent results of preliminary experimental investigations, and discusses practical design issues associated with parametrically excited MEM devices. The paper concludes in Section 8 with a summary of the present work and some comments on possible directions of future work in this area.

It should be noted that the bulk of this paper describes a detailed analysis of the governing equation of motion; this may be of interest to the nonlinear vibrations community, but of less direct interest to the MEMS community. Those readers not interested in the details of the analysis can focus on Section 2, in which the MEMS model is employed, and Section 7, which presents the general response features of parametrically excited MEMS, including an approach for evaluating and predicting the response features of these devices.

2. Parametrically excited MEM oscillators

The impetus of the present study was the analysis of single-degree-of-freedom (sdof) parametrically excited MEM oscillators, such as the one shown in Fig. 1. Such oscillators consist of a shuttle mass, namely the oscillator's backbone, B, connected to a substrate via four folded beam springs, S, and excited by a pair of non-interdigitated electrostatic comb drives, N, which are powered by a voltage source. These devices are

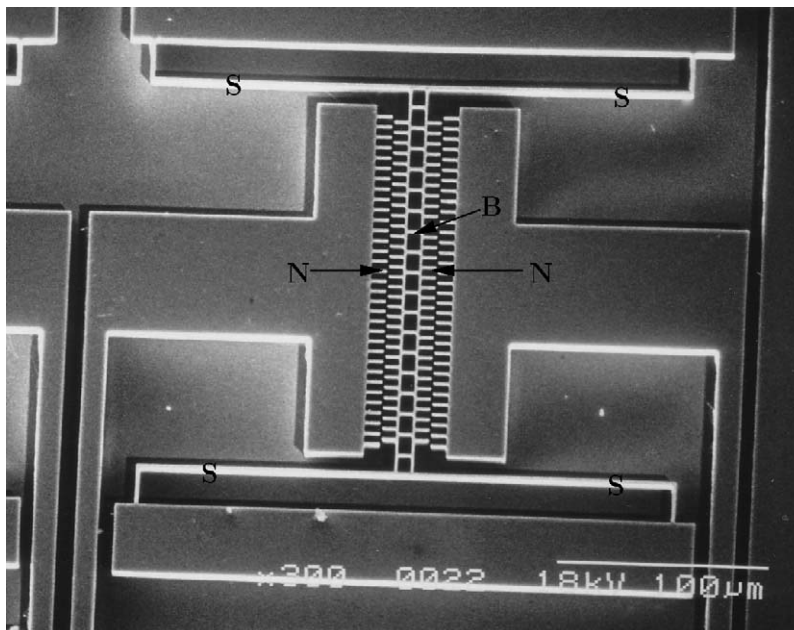


Fig. 1. A representative parametrically excited MEM oscillator. The oscillator's backbone is labeled B, S designates the mechanical beam springs, and N designates the non-interdigitated comb drives, which are used to provide the parametric excitation.

being proposed for use in a number of sensing and filtering applications [1,3,4]. Previous works, including those by the authors, have verified that these parametrically excited oscillators exhibit motion consistent with a rather simple-looking equation of motion, presented in Eq. (10) [1,3,5,6]. This is based on the following development.

To begin, the oscillator’s motion is assumed to be described by the movement of the shuttle mass in one direction. The forces acting on the system include those from the springs, the electrostatic forces from the comb drives, and a force that represents dissipative effects, which arise primarily from aerodynamic effects. These dissipative effects are generally small, especially when these devices are operated in a vacuum, and are typically modeled by a simple viscous damping force, although more complicated models have been proposed (see, for example, Refs. [7–10]). The resulting equation of motion is given by

$$m\ddot{x} + c\dot{x} + F_r(x) + F_{es}(x, t) = 0, \tag{1}$$

where $F_r(x)$ represents the elastic restoring force provided by the springs and $F_{es}(x, t)$ represents the electrostatic restoring and driving forces provided by the non-interdigitated electrostatic comb drives. As previous works have shown, the aforementioned forces can be accurately represented by cubic functions of displacement [1,3]. The restoring force from the mechanical springs is modeled by

$$F_r(x) = k_1x + k_3x^3, \tag{2}$$

where k_1 and k_3 are the effective linear and nonlinear spring coefficients from the beams. The electrostatic forces arising from the comb drives can accurately be modeled for small displacements as

$$F_{es}(x, t) = (r_{1A}x + r_{3A}x^3)V^2(t), \tag{3}$$

where r_{1A} and r_{3A} are electrostatic coefficients that depend on the physical dimensions of the electrostatic comb drives, and $V(t)$ is the voltage applied across the drives. In order to provide harmonic excitation to the device, an AC voltage of the form

$$V(t) = V_A\sqrt{1 + \cos \omega t} \tag{4}$$

is applied across the comb drives [1,3,6].

Substituting these forces back into Eq. (1) results in an equation of motion for the oscillator’s backbone of the form [1,6]:

$$m\ddot{x} + c\dot{x} + k_1x + k_3x^3 + (r_{1A}x + r_{3A}x^3)V_A^2(1 + \cos \omega t) = 0. \tag{5}$$

Time and displacement in Eq. (5) are rescaled according to

$$\tau = \omega_0 t, \tag{6}$$

where ω_0 is the purely elastic natural frequency defined as

$$\omega_0 = \sqrt{\frac{k_1}{m}} \tag{7}$$

and

$$z = \frac{x}{x_0}, \tag{8}$$

where x_0 is a characteristic length of the system (e.g. the length of the backbone). This scaling, assuming that the nondimensional damping, mechanical nonlinearities, and electrostatic forces are small (which is entirely consistent with the operation of such oscillators, especially near resonance), yields a nondimensional equation of motion of the form

$$z'' + 2\epsilon\zeta z' + z(1 + \epsilon\lambda_1 + \epsilon\lambda_1 \cos \Omega\tau) + \epsilon z^3(\chi + \lambda_3 + \lambda_3 \cos \Omega\tau) = 0, \tag{9}$$

where the new derivative operator and nondimensional parameters are defined as stated in Table 1 [1,6] and ϵ represents a “small” parameter introduced for analytical purposes.

The equation of motion considered in this work is a generalization of Eq. (9), wherein the effective stiffness and excitation coefficients (the λ ’s) are allowed to differ, in both the linear and nonlinear terms. This arises

Table 1
Nondimensional parameter definitions [1,6]

Definition	Nondimensional parameter
$(\bullet)' = \frac{d(\bullet)}{d\tau}$	Scaled time derivative
$\varepsilon\zeta = \frac{c}{2m\omega_0}$	Scaled damping ratio
$\varepsilon\lambda_1 = \frac{r_{1A}V_A^2}{k_1}$	Linear electrostatic excitation amplitude
$\Omega = \frac{\omega}{\omega_0}$	Nondimensional excitation frequency
$\varepsilon\chi = \frac{k_3x_0^2}{k_1}$	Nonlinear mechanical stiffness coefficient
$\varepsilon\lambda_3 = \frac{x_0^2r_{3A}V_A^2}{k_1}$	Nonlinear electrostatic excitation coefficient

naturally in the analysis of parametrically excited MEM oscillators with two sets of non-interdigitated comb drives, one of which provides an AC voltage, as described above, while the other provides a DC “bias” to the system. This “bias” does not offset the system equilibrium in the usual sense, but allows one to independently vary the effective electrostatic stiffness and excitation coefficients, resulting in Eq. (10). This arrangement of comb drives allows for more flexibility in tuning the response of such devices, so that designers can achieve certain desirable response features [1,5,6]. More generally, this governing equation of motion is representative of a number of parametrically excited dynamical systems, as highlighted in Refs. [11–13].

While works such as [1,3,5,6] examine the nonlinear dynamics of these parametrically excited MEM oscillators, their nonlinear response has not been fully explored, and a number of apparent anomalies have been observed in experimental investigations of these devices [2,3,14]. The analysis in the following sections provides a description for the entire range of possible responses for these systems (under the small damping and small response amplitude assumptions). This is followed by a specific example using the parameters from a device similar to that shown in Fig. 1.

One of the more interesting features of the equation of motion presented in Eq. (9) is that several of the coefficients of the equation, including the effective linear and nonlinear stiffnesses, depend on the amplitude of the AC voltage, V_A . This results in the fact that the qualitative nature of the system’s response generally depends on the amplitude of the excitation, and may differ for different input amplitudes. The analysis presented here describes a complete picture of this behavior, and provides designers of these devices with useful predictive tools. In Section 7, an example of this process and preliminary experimental results that verify the utility of the approach are given.

3. The equation of motion and perturbation analysis

The equation of motion of interest here is of the form

$$z'' + 2\varepsilon\zeta z' + z(1 + \varepsilon v_1 + \varepsilon\lambda_1 \cos \Omega\tau) + \varepsilon z^3(\gamma_3 + \lambda_3 \cos \Omega\tau) = 0, \quad (10)$$

where ε is a scaling parameter introduced for analysis and prime designates the derivative with respect to τ [1,5,6,15,16]. Note that this is a special case of generalized parametric excitation in that there is not a phase difference in the excitation seen by the linear and nonlinear terms. However, in many systems the excitation arises from a single source, resulting in zero phase difference (see, for example, Refs. [11–13,17,18]). This is the case for the present study, and this equation proves sufficient for capturing the dynamic response of the MEM devices under consideration.

The method of averaging is employed to analyze Eq. (10). To aid this, a standard coordinate transformation is introduced to convert the equation to amplitude and phase coordinates, namely,

$$z(\tau) = a(\tau) \cos\left(\frac{\Omega\tau}{2} + \psi(\tau)\right), \tag{11}$$

$$z'(\tau) = -a(\tau) \frac{\Omega}{2} \sin\left(\frac{\Omega\tau}{2} + \psi(\tau)\right). \tag{12}$$

Note that this conversion requires that a certain constraint equation involving a' and ψ' be satisfied, just as in the method of variation of parameters; see, for example, Ref. [19]. In order to capture the dynamics near the principal parametric resonance, an excitation frequency detuning parameter σ is introduced, defined by,

$$\Omega = 2 + \varepsilon\sigma, \tag{13}$$

where σ measures the closeness of the excitation frequency to the principal parametric resonance condition. Averaging the resulting equations, now in terms of amplitude and phase coordinates, over the period $4\pi/\Omega$ in the τ -domain produces the system's averaged equations [1,5,6]. These are given by

$$a' = \frac{1}{8}\varepsilon[-8\zeta + (2\lambda_1 + a^2\lambda_3) \sin 2\psi] + \mathcal{O}(\varepsilon^2), \tag{14}$$

$$\psi' = \frac{1}{8}\varepsilon[3a^2\gamma_3 + 4v_1 - 4\sigma + 2(\lambda_1 + a^2\lambda_3) \cos 2\psi] + \mathcal{O}(\varepsilon^2). \tag{15}$$

Note that the presence of parametric excitation in the cubic term, captured by the parameter λ_3 , introduces additional coupling in these equations that is not present in the case of purely linear parametric excitation. Consequently, the nontrivial steady-state solutions of the system take on a more complicated form and the system has much more interesting response characteristics.

4. Steady-state responses, their stability, and their effective nonlinearities

Since the characteristic form of the system nonlinearity (i.e., hardening or softening) is a critical feature of the response for current purposes, and this is largely unaffected by damping, zero damping ($\zeta = 0$) is assumed to simplify the analysis. (Note that while closed-form solutions are obtainable for nonzero damping, they are inherently complicated, and thus not well suited for detailed analysis or easy interpretation.) We will consider the effects of small damping subsequently. Steady-state responses are captured by setting $(a', \psi') = (0, 0)$. Examining the resulting equations reveals that the system has a trivial solution and three distinct sets of nontrivial solution branches. The first two nontrivial sets appear in pairs with amplitudes and associated phases given by

$$a_1 = \pm \sqrt{\frac{4\sigma + 2\lambda_1 - 4v_1}{3\gamma_3 - 2\lambda_3}}, \tag{16}$$

$$\psi_1 = \frac{\pi}{2}, \tag{17}$$

and

$$a_2 = \pm \sqrt{\frac{4\sigma - 2\lambda_1 - 4v_1}{3\gamma_3 + 2\lambda_3}}, \tag{18}$$

$$\psi_2 = 0. \tag{19}$$

Note that each \pm pair represents the same physical response; they appear this way due to the phase relation of this subharmonic response relative to the excitation. Likewise, all responses with magnitude π phase shifts represent the same physical response, and thus are not included. For each of these solutions, the signs of the terms under the square root determine the frequency range over which these branches are real valued, and thus physically meaningful. The numerators of these terms are dictated by linear frequency terms, and the

denominators are set by nonlinear terms. Of direct interest here is the role played by the nonlinearities, which differ for each of these frequency-dependent branches. To describe these effects, effective nonlinearities η_1 and η_2 are defined that dictate the behavior of these branches. These nonlinearities are taken from the denominator of the expressions above and are given by [1,5]

$$\eta_1 = 3\gamma_3 - 2\lambda_3 \tag{20}$$

and

$$\eta_2 = 3\gamma_3 + 2\lambda_3. \tag{21}$$

The case $\eta_1 < 0$ and $\eta_2 < 0$ results in the usual softening nonlinearity. Likewise, the usual hardening nonlinearity occurs for $\eta_1 > 0$ and $\eta_2 > 0$. However, due to the nature of this equation of motion, two mixed cases also exist, namely, $\eta_1 > 0$ and $\eta_2 < 0$, and $\eta_1 < 0$ and $\eta_2 > 0$, which correspond to the two branches delineated in Eqs. (16) and (18) bending toward or away from one another, as determined by λ_1 and ν_1 . This result is summarized in Fig. 2, which delineates the various response regions within the γ_3 - λ_3 parameter space. Note that a transition between response types occurs when one or both of the effective nonlinearities equals zero, in which case the bifurcation associated with crossing the boundary of the parametric instability (given by an Arnold tongue) becomes degenerate. Accordingly, phenomena near these degeneracies cannot be captured without the inclusion of high-order nonlinear terms, which are not considered here.

The solutions for the third set of nontrivial responses have constant amplitude (for zero damping) and are given, with their phase, by

$$a_3 = \pm \sqrt{\frac{-2\lambda_1}{\lambda_3}}, \tag{22}$$

$$\psi_3 = \pm \frac{1}{2} \arccos\left(\frac{-3\gamma_3\lambda_1 + 2\lambda_3\nu_1 - 2\lambda_3\sigma}{\lambda_1\lambda_3}\right). \tag{23}$$

Note that there will be four such solutions, only two of which will be physically distinct (as evident in the next section), corresponding to each branch of the respective inverse cosine function. Accordingly, these solutions will appear in either the upper or lower half-plane of the parameter space delineated in Fig. 2, as dictated by the sign of λ_1 . As such, the system undergoes a bifurcation across the $\lambda_3 = 0$ axis in Fig. 2, which corresponds to the creation or annihilation of the constant amplitude solution. It should be noted however, that this creation (or annihilation) is a “smooth” process, as the solution appears from positive or negative infinity due to the presence of λ_3 in the solution’s denominator. As will be shown shortly, the presence of these additional solution branches significantly complicates the system’s dynamics within certain parameter regimes, especially

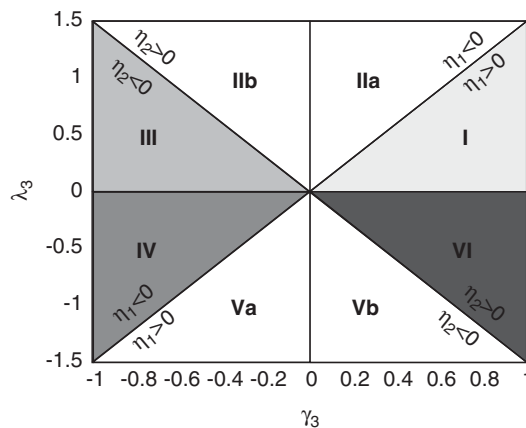


Fig. 2. The γ_3 - λ_3 parameter space [1]. Those regions designated I and VI exhibit hardening (or quasi-hardening) nonlinear characteristics, those designated III and IV exhibit softening (or quasi-softening) nonlinear characteristics, and those designated IIa, IIb, Va, and Vb exhibit mixed nonlinear characteristics.

when viewed from a frequency response perspective. Before turning to the generation of frequency response curves, the stability of the various response branches is first determined.

Though the local stability of steady-state responses is generally addressed by considering the local linear behavior of the averaged equations near the steady-state responses in the (a, ψ) polar coordinate space, singularities at the origin require that a coordinate change be introduced. As such, the following coordinate change is evoked, which converts the polar coordinates (a, ψ) into Cartesian coordinates (x, y) :

$$x(\tau) = a(\tau) \cos[\psi(\tau)], \tag{24}$$

$$y(\tau) = a(\tau) \sin[\psi(\tau)]. \tag{25}$$

This coordinate change results in averaged equations of the form

$$x' = \frac{1}{8} \varepsilon [(2\lambda_1 - 4\nu_1 + 4\sigma)y - 3\gamma_3 x^2 y + (-3\gamma_3 + 2\lambda_3)y^3 - 8\zeta x] + \mathcal{O}(\varepsilon^2), \tag{26}$$

$$y' = \frac{1}{8} \varepsilon [(2\lambda_1 + 4\nu_1 - 4\sigma)x + 3\gamma_3 x y^2 + (3\gamma_3 + 2\lambda_3)x^3 - 8\zeta y] + \mathcal{O}(\varepsilon^2). \tag{27}$$

Using these equations, with $\zeta = 0$, local stability results are inferred by considering the response of the system when linearized about the steady states. Letting the state vector be

$$X(\tau) = \begin{bmatrix} x(\tau) \\ y(\tau) \end{bmatrix} \tag{28}$$

and the steady-state values be given by

$$X^* = \begin{bmatrix} x^* \\ y^* \end{bmatrix}, \tag{29}$$

the local linearized equation of motion for the system can be written as

$$Y'(\tau) = J|_{X^*} Y(\tau), \tag{30}$$

where

$$Y(\tau) = X(\tau) - X^* \tag{31}$$

and J is the Jacobian matrix of the averaged equations, Eqs. (26) and (27), evaluated at steady state, X^* . The stability of the steady-state response is governed by the eigenvalues of the corresponding Jacobian.

To simplify the analysis, we will consider the stability in terms of the trace and determinant of the 2×2 Jacobian [20]. In particular, the eigenvalues can be expressed in terms of the trace, T , and the determinant, Δ , as

$$\Lambda_{1,2} = \frac{1}{2}(T \pm \sqrt{T^2 - 4\Delta}). \tag{32}$$

For the undamped case under consideration here, the trace of the Jacobian for each of the steady-state responses is zero, thus only two generic equilibrium types are possible for nontrivial eigenvalues: saddles (unstable) and centers (marginally stable). Which of these equilibrium types exists depends solely on the sign of the determinant. In particular, when $\Delta > 0$ the equilibrium is a center, and when $\Delta < 0$ the equilibrium is a saddle. The remaining case, $\Delta = 0$, corresponds to the degenerate case of two identically zero eigenvalues, and as such is used here only to identify where stability changes occur.

The trivial solution features a determinant of the form

$$\Delta_0 = -\frac{1}{16} \varepsilon^2 [\lambda_1^2 - 4(\nu_1 - \sigma)^2]. \tag{33}$$

By finding the roots of $\Delta_0 = 0$, the critical frequency values (detuning values) at which stability changes occur can be shown to be

$$\sigma_1 = \nu_1 - \frac{\lambda_1}{2} \tag{34}$$

and

$$\sigma_2 = v_1 + \frac{\lambda_1}{2}, \quad (35)$$

respectively. The stability in each frequency and detuning region is then determined by evaluating the determinant at a single point within the domain or by calculating the derivative of the determinant at the critical frequency value. This shows that the trivial solution appears as a center for $\sigma < \min(\sigma_1, \sigma_2)$ and $\sigma > \max(\sigma_1, \sigma_2)$, and as a saddle for $\min(\sigma_1, \sigma_2) < \sigma < \max(\sigma_1, \sigma_2)$. These results are, of course, unaffected by the nonlinear excitation term and are closely related to the results obtained for a standard Mathieu equation. The distinct difference here, however, is that “wedge of instability” which appears in the λ_1 – Ω parameter space is generally distorted away from the typical configuration seen in Refs. [21,22], for example, due to the presence of the frequency-shifting v_1 term (this is considered extensively in Ref. [1]).

Using similar techniques, the constant amplitude solutions of Eq. (22) can be shown to be saddles for all frequency values where the solutions exist, as determined by considering parameter values where their phases are real-valued. It is found that these solutions exist between the detuning values

$$\sigma = \frac{-3\lambda_1\gamma_3 - \lambda_1\lambda_3 + 2\lambda_3v_1}{2\lambda_3} \quad (36)$$

and

$$\sigma = \frac{-3\lambda_1\gamma_3 + \lambda_1\lambda_3 + 2\lambda_3v_1}{2\lambda_3}. \quad (37)$$

Note that each of these values may serve as an upper or lower bound, depending on the sign of λ_1 .

The remaining two branches are slightly more complicated in that their stability is heavily dependent on which region of the γ_3 – λ_3 parameter space (see Fig. 2) the system falls within. Regardless, the stability for each of the branches can be found by evoking the fact that the response branch presented in Eq. (16) has a determinant given by

$$\Delta = \frac{\varepsilon^2(\lambda_1 - 2v_1 + 2\sigma)(3\lambda_1\gamma_3 - \lambda_1\lambda_3 - 2\lambda_3v_1 + 2\lambda_3\sigma)}{12\gamma_3 - 8\lambda_3}, \quad (38)$$

which features critical frequency values of

$$\sigma = v_1 - \frac{\lambda_1}{2}, \quad (39)$$

corresponding to the bifurcation at which this branch emanates from the origin, and

$$\sigma = \frac{-3\lambda_1\gamma_3 + \lambda_1\lambda_3 + 2\lambda_3v_1}{2\lambda_3}, \quad (40)$$

corresponding to the bifurcation which connects this branch to the constant amplitude branches. The response branch presented in Eq. (18) has a determinant given by

$$\Delta = \frac{\varepsilon^2(\lambda_1 + 2v_1 - 2\sigma)(3\lambda_1\gamma_3 + \lambda_1\lambda_3 - 2\lambda_3v_1 + 2\lambda_3\sigma)}{12\gamma_3 + 8\lambda_3}, \quad (41)$$

which features critical frequency values of

$$\sigma = v_1 + \frac{\lambda_1}{2}, \quad (42)$$

corresponding to the bifurcation at which this branch emanates from the origin, and

$$\sigma = \frac{-3\lambda_1\gamma_3 - \lambda_1\lambda_3 + 2\lambda_3v_1}{2\lambda_3}, \quad (43)$$

corresponding to the bifurcation which connects this branch to the constant amplitude branches.

Combining these results with the steady-state solutions derived above yields a complete picture of the oscillator’s possible frequency responses, as described in detail in Section 5.

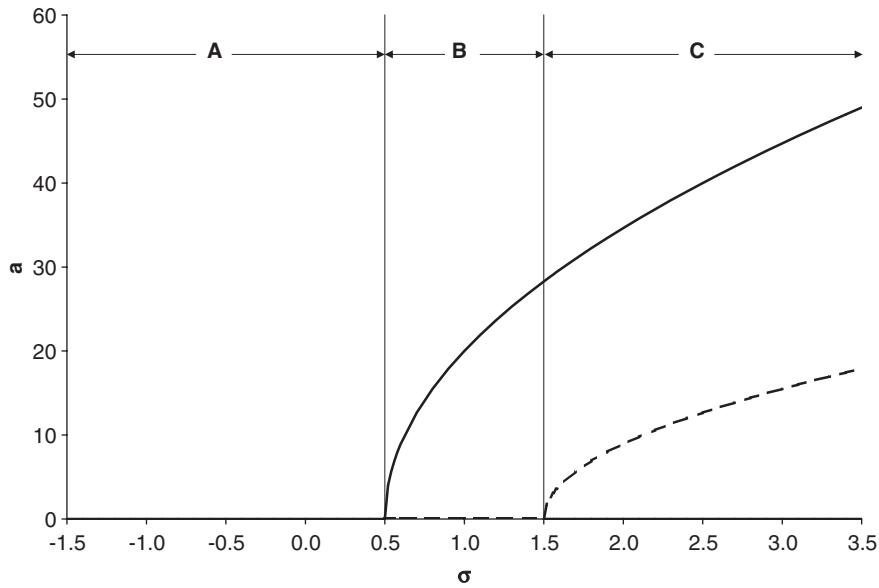


Fig. 3. Representative frequency response plot showing response amplitude versus frequency detuning for Region I ($\gamma_3 = 0.005$, $\lambda_3 = 0.005$) in Fig. 2. Note the response’s hardening nonlinear characteristics. Also note that here, as well as in Figs. 4–14, solid lines indicate stable response branches and dashed lines unstable response branches.

5. System frequency responses

To facilitate understanding of the analysis presented in Section 4, consider a representative sdof dynamical system modeled by Eq. (10). In particular, consider an undamped version ($\zeta = 0$) with $\nu_1 = \lambda_1 = 1$. (The results can easily be extended for other values of ν_1 and λ_1 , both positive and negative.) By applying the results of the aforementioned section to this typical case, frequency response plots, such as those shown in Figs. 3–14, are easily generated for each of the regions depicted in Fig. 2. A brief explanation of each of these plots follows.

To begin, consider the amplitude versus frequency response curves depicted in Figs. 3 and 6, corresponding to Regions I and III in Fig. 2, respectively. As a quick examination reveals, these regions appear consistent with normal softening and hardening nonlinear behavior. That is, the nontrivial solutions branch off in two distinct pitchfork bifurcations, one subcritical and the other supercritical, and all solutions remain globally bounded. (Note that the term globally bounded is used here to designate the fact that all initial conditions result in bounded responses.) Though not shown, the phase response will be equally mundane in that it remains constant across the branches, as dictated by Eqs. (17) and (19). The frequency responses shown in Figs. 4 and 5, corresponding to the topologically equivalent regions labeled IIa and IIb in Fig. 2, are slightly more interesting.¹ Here the nontrivial solutions also branch off, but in each instance a subcritical bifurcation occurs. The net result is that the two response curves actually bend away from one another and some solutions are globally unbounded (specifically, all nonzero initial conditions lead to unbounded motions over the frequency range where the trivial solution is unstable, and where the trivial solution is stable, initial conditions with sufficiently large energies lead to unbounded responses). Of course, here, and elsewhere, these “globally unbounded” solutions will be bounded by higher-order nonlinear effects not included here. The phase responses of the solutions within these regions, much like those considered above, remain invariant in frequency and thus are omitted.

¹Note that these regions are given different designations only due to the fact that the nontrivial response branches to the left and right of the resonance have different amplitudes, which are reversed in these two regions. This is not physically important, since both branches are unstable. However, in other regions, this distinction will have consequences in terms of the observed frequency response behavior.

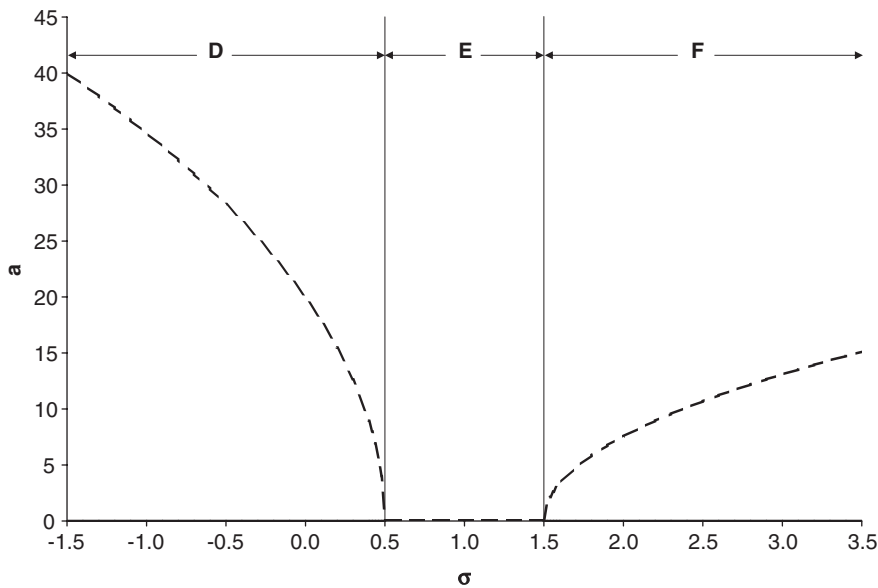


Fig. 4. Representative frequency response plot showing response amplitude versus frequency detuning for Region IIa ($\gamma_3 = 0.005$, $\lambda_3 = 0.010$) in Fig. 2. Note the response's mixed nonlinear characteristics.

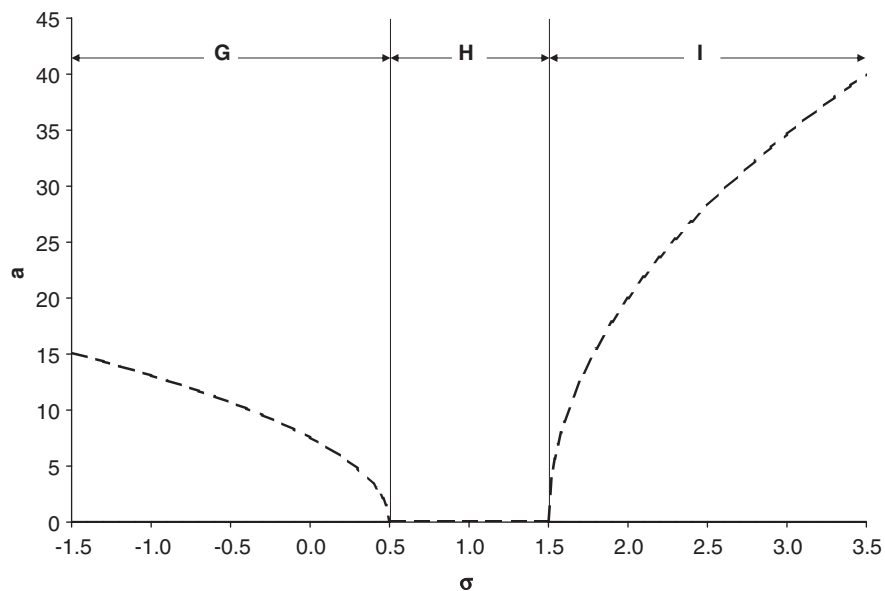


Fig. 5. Representative frequency response plot showing response amplitude versus frequency detuning for Region IIb ($\gamma_3 = -0.005$, $\lambda_3 = 0.010$) in Fig. 2. Note the response's mixed nonlinear characteristics.

In the lower half-plane of the parameter space depicted in Fig. 2, the existence of the additional nontrivial, constant amplitude, solutions complicates matters. First, consider Figs. 7 and 13, corresponding to Regions IV and VI in Fig. 2, respectively. Here the near zero amplitude responses resemble those of Figs. 3 and 6, respectively. However, as the frequency is swept further away from zero detuning ($\sigma = 0$), the system undergoes two additional local bifurcations, corresponding to the creation and annihilation of the constant amplitude response, which connects the other two nontrivial branches. Though this still results in a globally

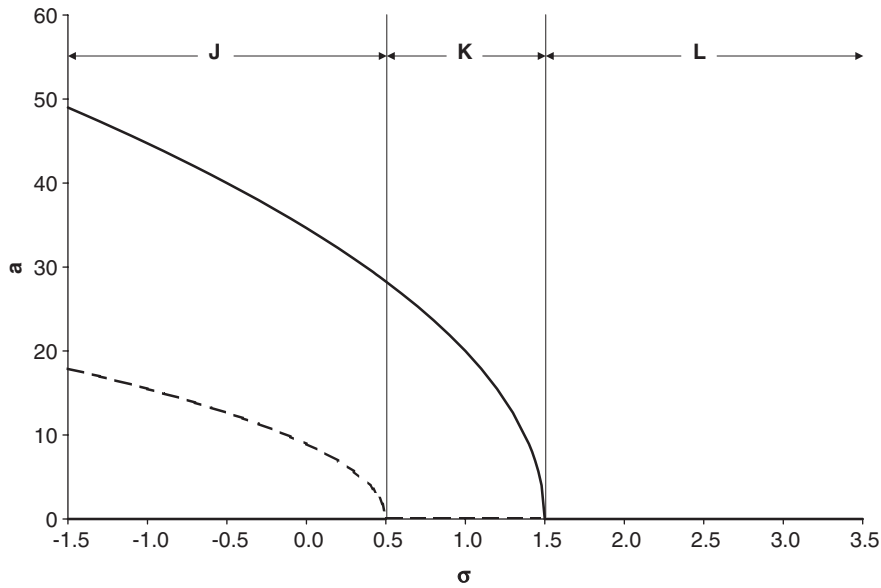


Fig. 6. Representative frequency response plot showing response amplitude versus frequency detuning for Region III ($\gamma_3 = -0.005$, $\lambda_3 = 0.005$) in Fig. 2. Note the response's softening nonlinear characteristics.

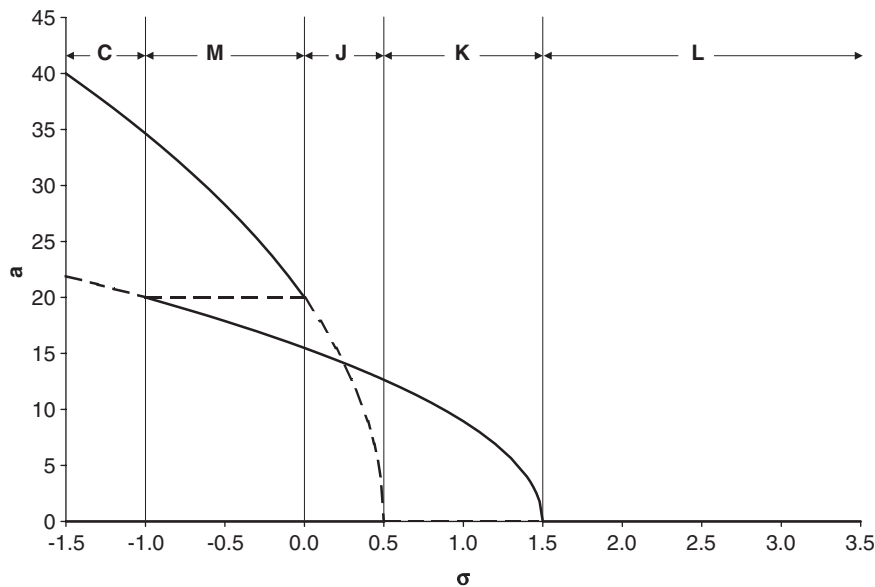


Fig. 7. Representative frequency response plot showing response amplitude versus frequency detuning for Region IV ($\gamma_3 = -0.005$, $\lambda_3 = -0.005$) in Fig. 2. Note the response's quasi-softening nonlinear characteristics.

bounded system with quasi-softening or hardening characteristics, it is distinct from the usual hardening and softening response curves of the upper half-plane, due to the fact that the stability in the two nonconstant branches switches via the constant amplitude branch. This switching can be further reconciled by considering the phase response plots shown in Figs. 8 and 14, which show the transition from one phase to another as the constant amplitude branch is traversed.

The responses shown in Figs. 9 and 11, corresponding to the regions labeled Va and Vb in Fig. 2, are also quite interesting. Again, the response features four distinct local bifurcations, two of the pitchfork variety

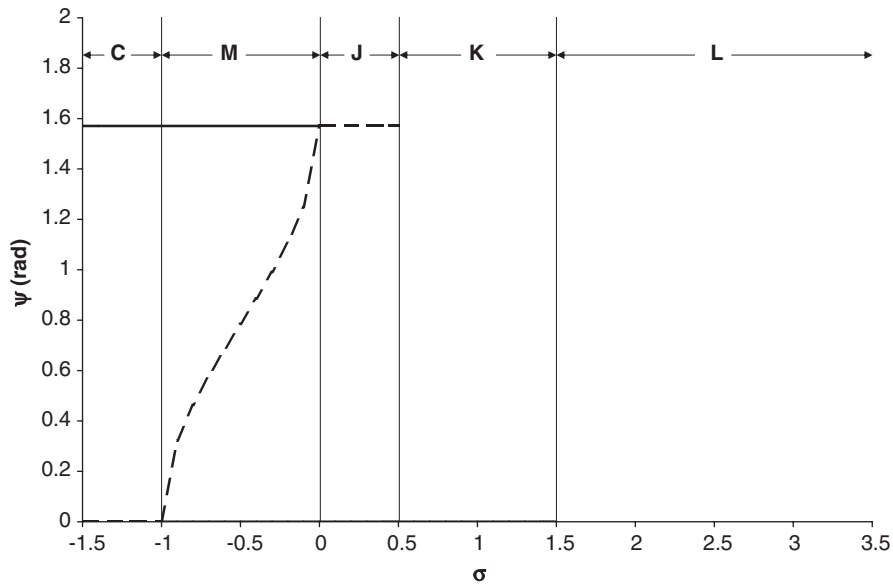


Fig. 8. Representative frequency response plot showing phase angle versus frequency detuning for Region IV ($\gamma_3 = -0.005$, $\lambda_3 = -0.005$) in Fig. 2.

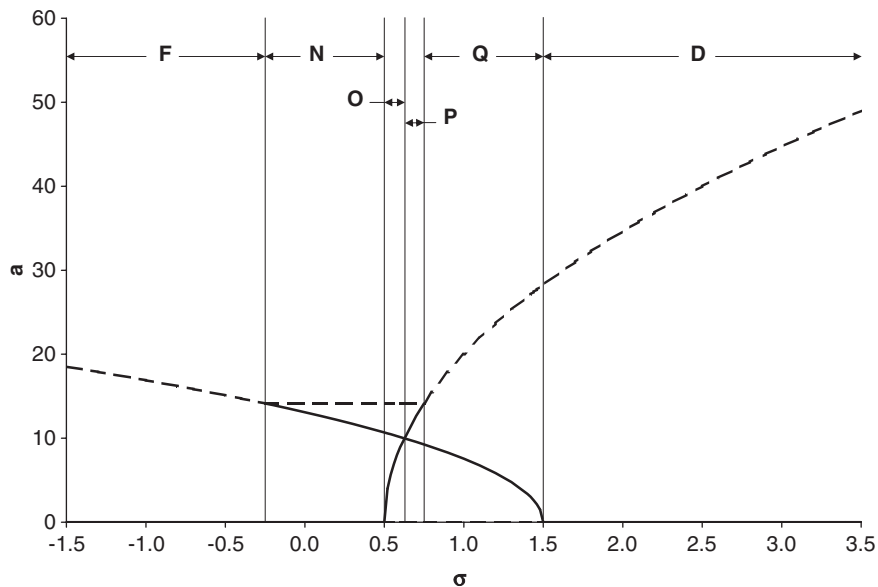


Fig. 9. Representative frequency response plot showing response amplitude versus frequency detuning for Region Va ($\gamma_3 = -0.005$, $\lambda_3 = -0.010$) in Fig. 2. Note the response's mixed nonlinear characteristics.

where the nontrivial solutions branch off from zero, and two corresponding to the creation and annihilation of the constant amplitude solution, again connecting the other two nontrivial branches. The net result is a globally unbounded system (that is, sufficiently large initial energies will lead to unbounded responses) with nontrivial response branches which bend towards one another and are both initially stable. Both of these branches lose stability via bifurcations where they connect with the constant amplitude branch. It should also be noted that a global bifurcation, in particular, a saddle connection, occurs within these two regimes as well.

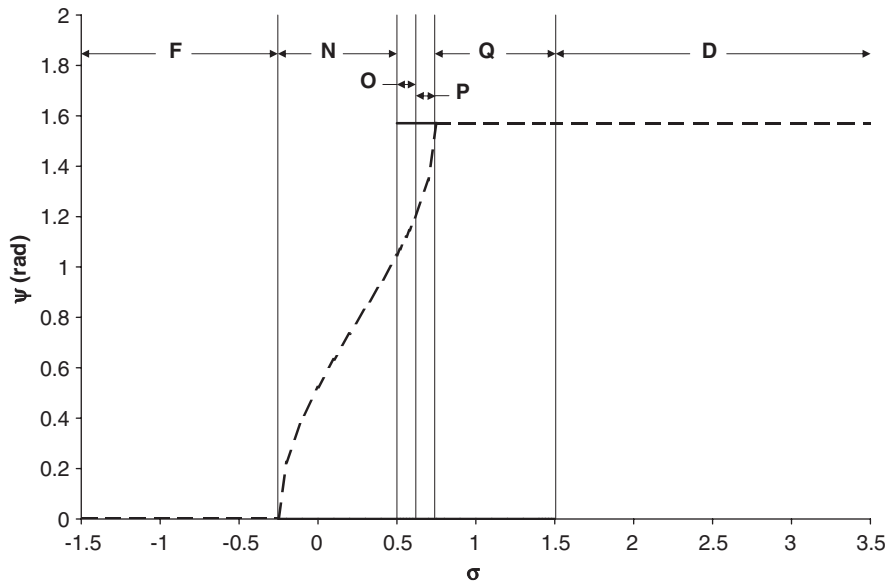


Fig. 10. Representative frequency response plot showing phase angle versus frequency detuning for Region Va ($\gamma_3 = -0.005$, $\lambda_3 = -0.010$) in Fig. 2.

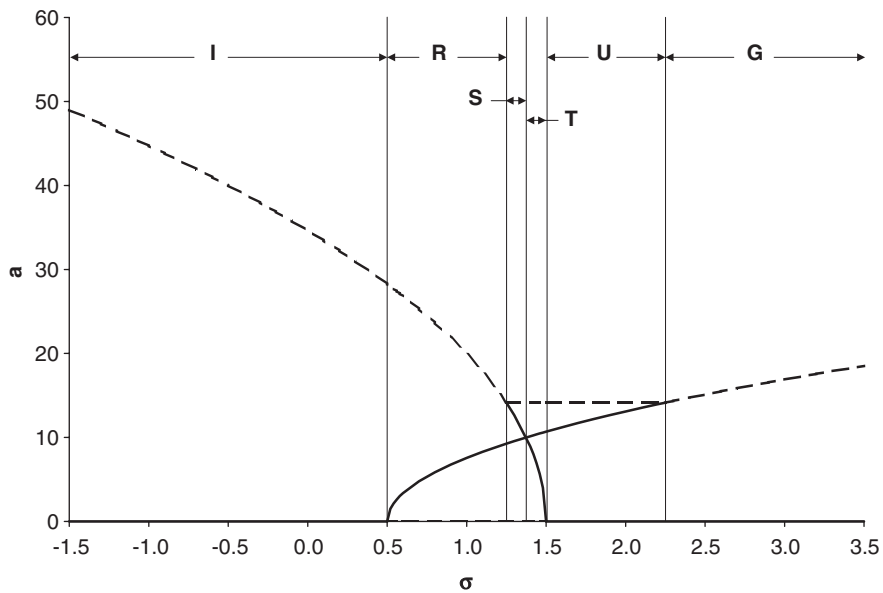


Fig. 11. Representative frequency response plot showing response amplitude versus frequency detuning for Region Vb ($\gamma_3 = 0.005$, $\lambda_3 = -0.010$) in Fig. 2. Note the response's mixed nonlinear characteristics.

This can be verified geometrically by considering the phase portraits presented in Fig. 15 below, which clearly show the connection of the manifolds originating from the saddle at the origin with the manifolds originating from the saddles corresponding to the constant amplitude solutions. This can also be confirmed analytically by performing a simple invariant manifold calculation. In particular, it is observed that when the saddle connections exist, they are linear manifolds, and the attendant x and y dynamics of the system at the specified

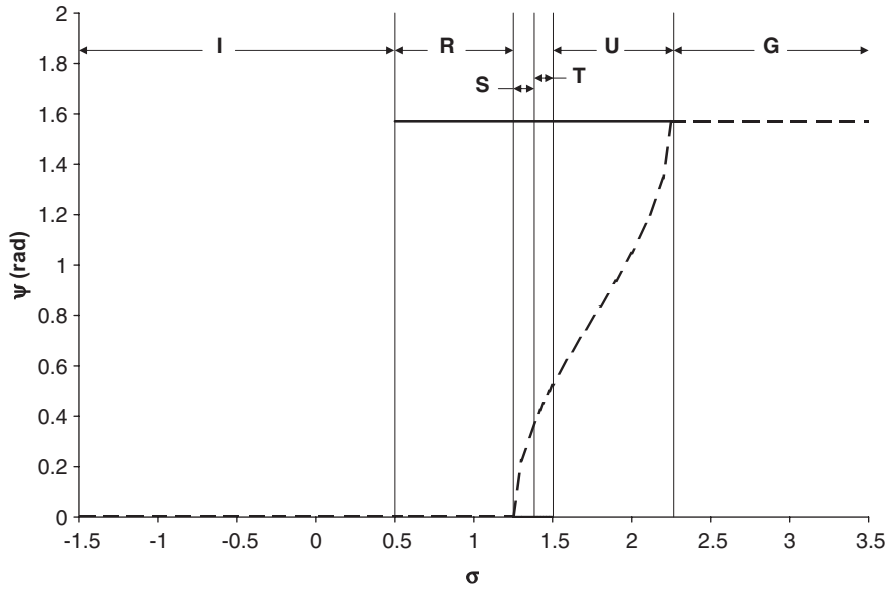


Fig. 12. Representative frequency response plot showing phase angle versus frequency detuning for Region Vb ($\gamma_3 = 0.005$, $\lambda_3 = -0.010$) in Fig. 2.

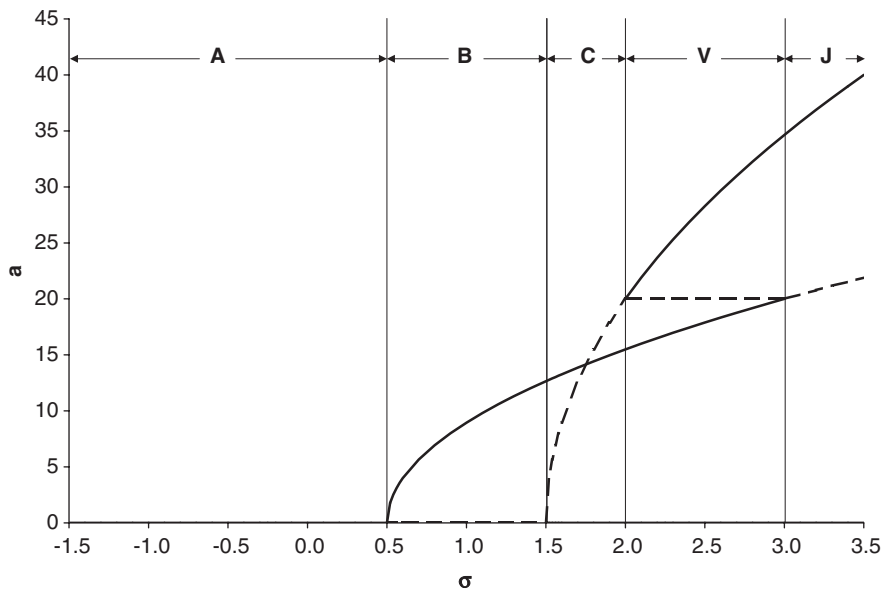


Fig. 13. Representative frequency response plot showing response amplitude versus frequency detuning for Region VI ($\gamma_3 = 0.005$, $\lambda_3 = -0.005$) in Fig. 2. Note the response’s quasi-hardening nonlinear characteristics.

bifurcation point can be related according to

$$y = \alpha x \tag{44}$$

and

$$y' = \alpha x', \tag{45}$$

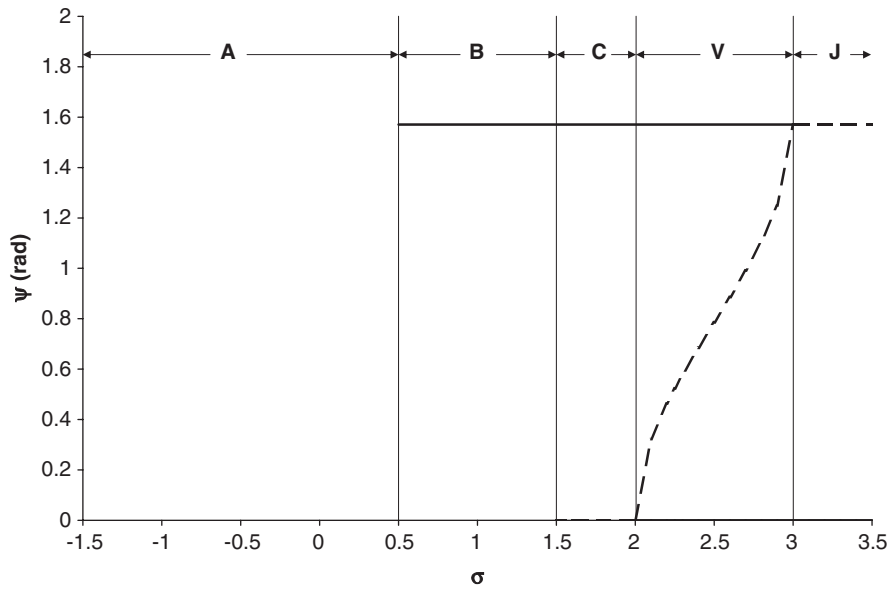


Fig. 14. Representative frequency response plot showing phase angle versus frequency detuning for Region VI ($\gamma_3 = 0.005$, $\lambda_3 = -0.005$) in Fig. 2.

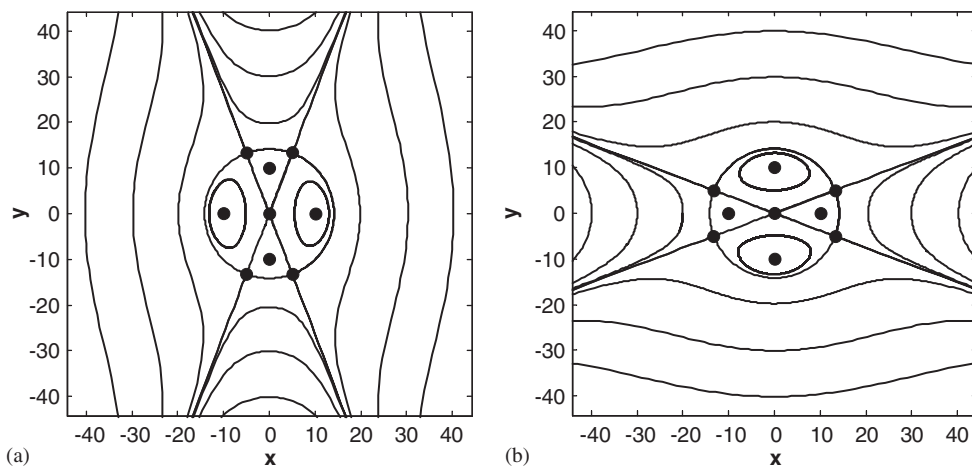


Fig. 15. Representative phase planes corresponding to the frequency (detuning) boundaries (a) OP and (b) ST where the saddle connection global bifurcations occur.

where α is a to be determined constant that represents the slopes of the saddle-connection invariant manifolds. Substituting these relationships into the undamped versions of Eqs. (26) and (27) and equating like powers of x (or y) yields both a constraint on the magnitude of α and a frequency, or more accurately, a detuning condition, at which the bifurcation occurs. In particular, it can be shown that the global bifurcation occurs for

$$\sigma = \frac{-3\gamma_3\lambda_1 + 4\lambda_3\nu_1}{4\lambda_3}, \tag{46}$$

which interestingly enough also corresponds to the frequency value at which the two stable nontrivial branches “intersect” in the specified amplitude versus frequency response plots (for Regions Va and Vb). It should be noted that the phase dynamics within these regions follow the general trends outlined above for Regions IV and VI.

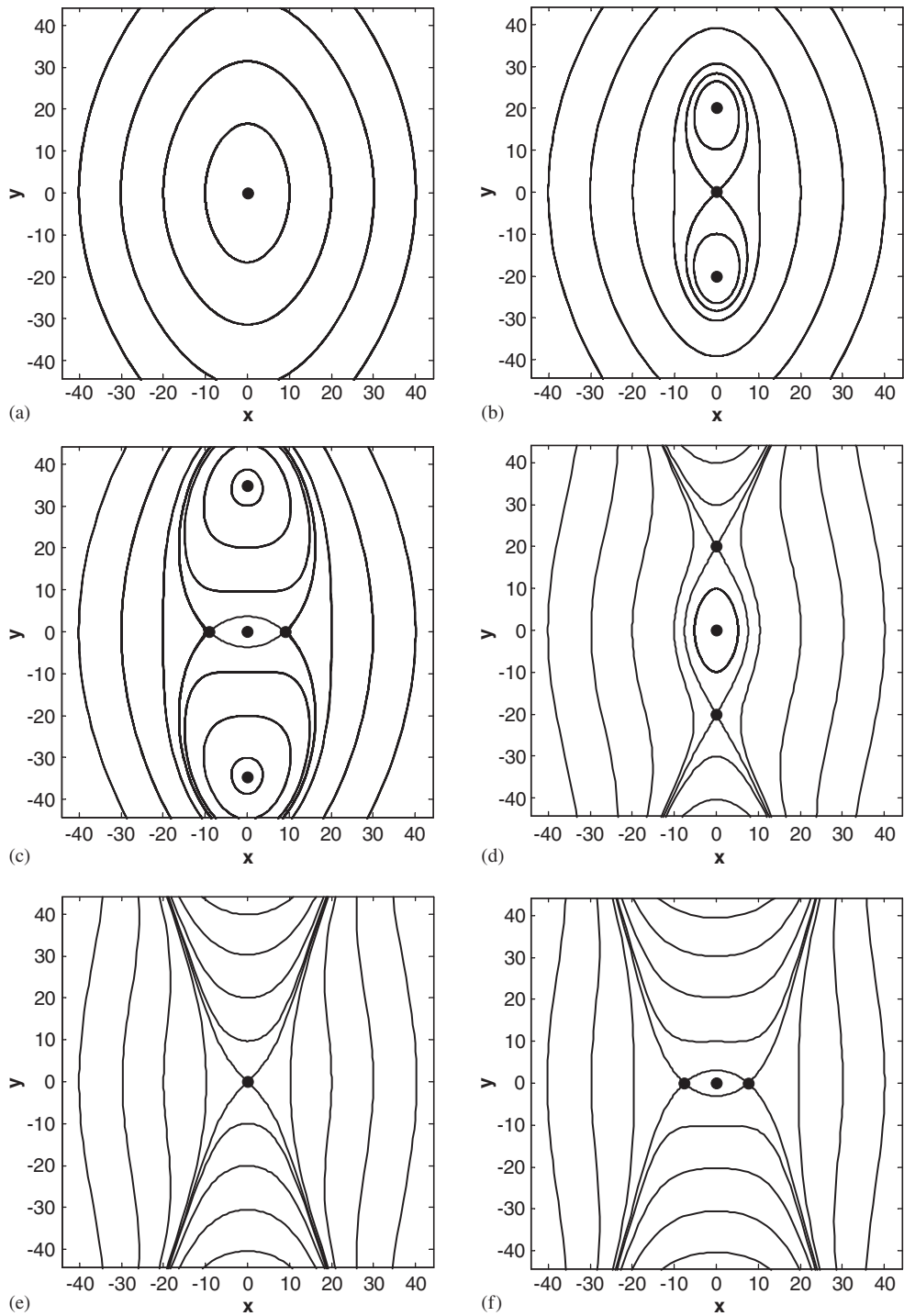


Fig. 16. Representative phase planes corresponding to (a) Region A, (b) Region B, (c) Region C, (d) Region D, (e) Region E, and (f) Region F in Figs. 3–14.

To provide additional insight into the bifurcations described above, representative phase planes corresponding to each of the frequency response regimes delineated in Figs. 3–14 are presented. These plots, corresponding to the conservative system explored in this section, are shown in

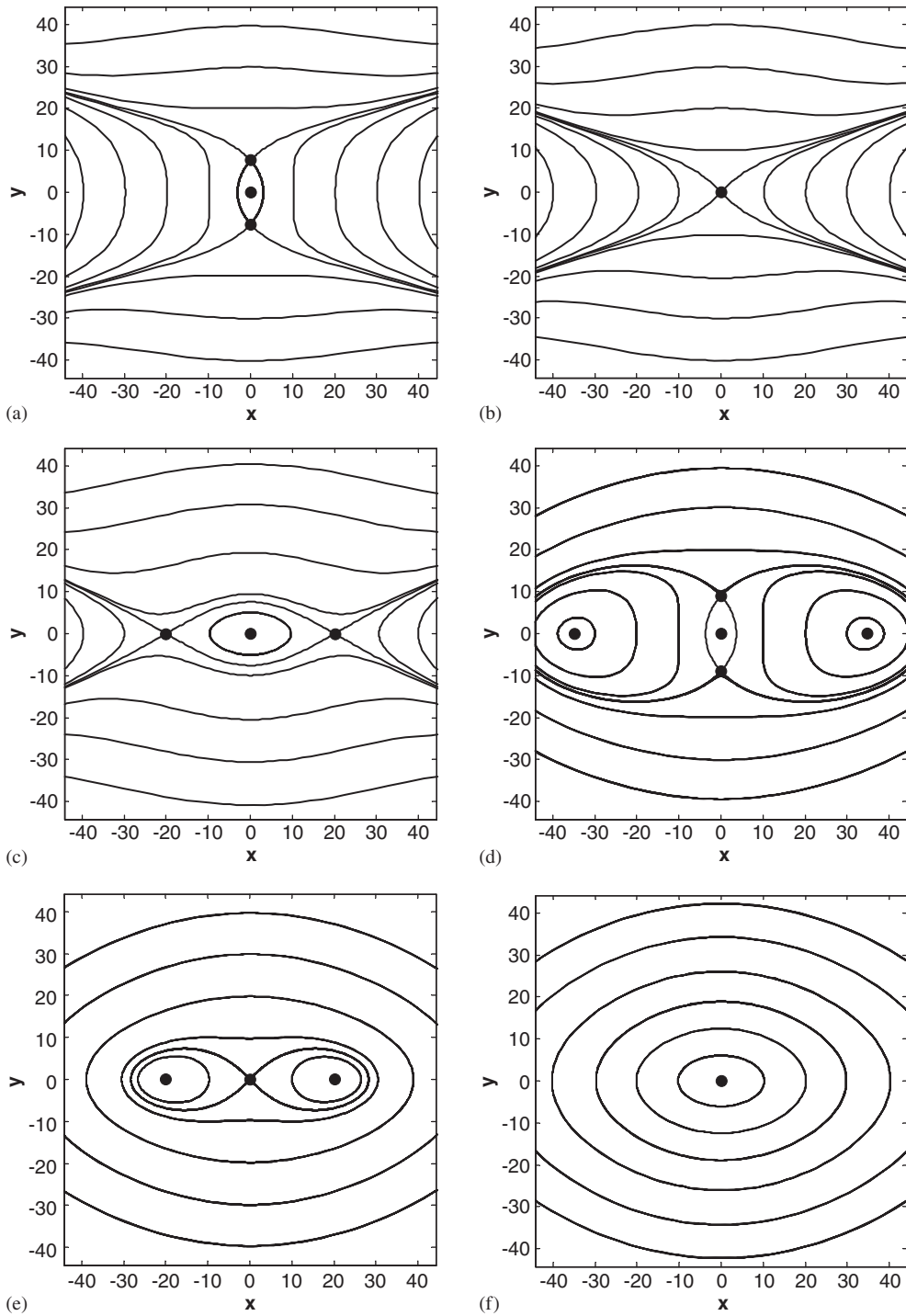


Fig. 17. Representative phase planes corresponding to (a) Region G, (b) Region H, (c) Region I, (d) Region J, (e) Region K, and (f) Region L in Figs. 3–14.

Figs. 15–19. Note that the capital letters designate topologically distinct phase portraits, and that these are associated with the similarly labeled frequency ranges in the frequency response plots shown in Figs. 3–14.

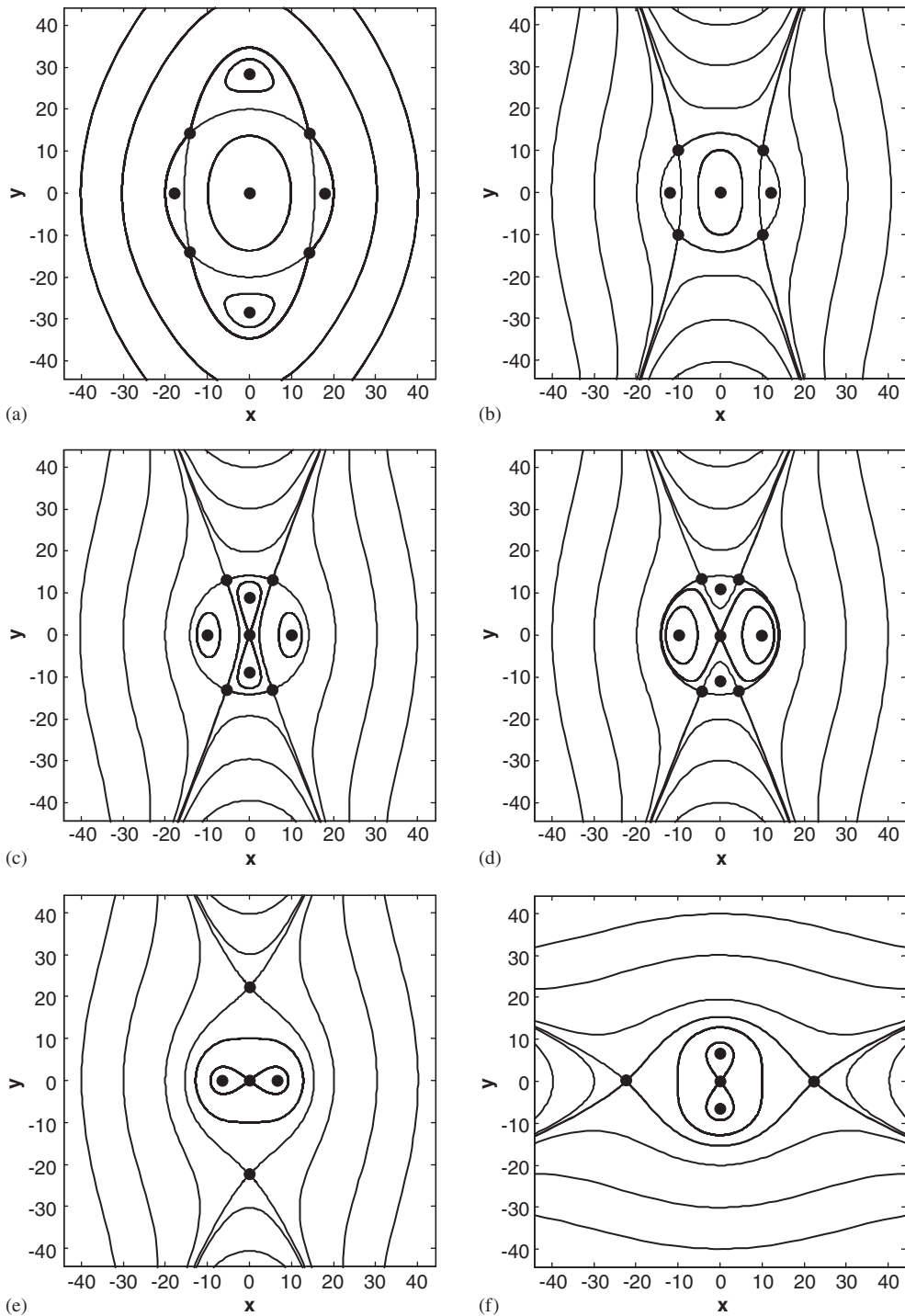


Fig. 18. Representative phase planes corresponding to (a) Region M, (b) Region N, (c) Region O, (d) Region P, (e) Region Q, and (f) Region R in Figs. 3–14.

While the results presented above are for a special case of the equation of motion in question, it should be noted, as previously mentioned, that the results are easily extendible for arbitrary v_1 and λ_1 . In particular, other values of these parameters typically result in two notable differences. First, selecting different values for

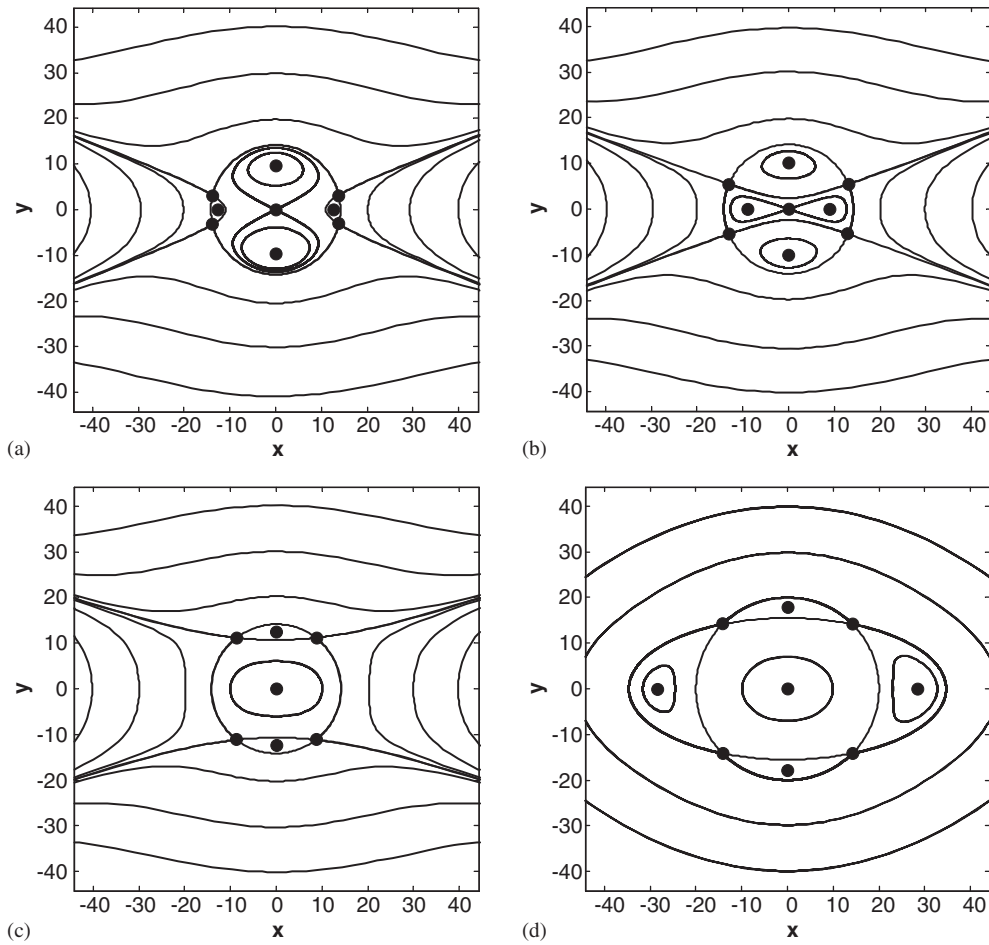


Fig. 19. Representative phase planes corresponding to (a) Region S, (b) Region T, (c) Region U, and (d) Region V in Figs. 3–14.

v_1 and λ_1 results in a distortion of the Arnold tongue associated with the stability of the solution’s trivial solution. This is easily reconciled through consideration of Eqs. (34) and (35). In addition, specifying the value of λ_1 to be negative results in a symmetric reflection of the γ_3 – λ_3 parameter space about the $\lambda_3 = 0$ axis. This can be reconciled by noting that the existence of a_3 depends on the sign of the ratio λ_1/λ_3 , and thus for $\lambda_1 < 0$ the constant amplitude solutions will appear in the upper half-plane of the parameter space instead of the lower half-plane.

It should also be noted that, in addition to the phenomena described above, the system exhibits a number of additional interesting features. First, note that in the absence of damping the phase portraits show a distinct symmetry. The breaking of this symmetry is considered in the following section, where the effects of small system damping on the system response are considered. Also, and related to the symmetry, over certain frequency (detuning) ranges, an invariant circle exists, given by

$$x^2 + y^2 = \frac{-2\lambda_1}{\lambda_3}. \tag{47}$$

Note that the radius of this circle corresponds to the magnitude of the constant amplitude branches and, therefore, these solutions lie on this invariant circle. Furthermore, these solutions are connected to one another via invariant manifolds consisting of circular arcs.

These analytical results, and the graphical representations expressed in terms of frequency response curves and phase portraits, give a complete picture of the response of the system for zero damping. Small damping will destroy the symmetry that permits such a thorough analysis, but the resulting responses can be inferred by

straightforward extrapolations of the undamped results. Steps in this direction, including results from numerical analysis of the damped equations of motion, are considered in the next section.

6. The effects of damping

Thus far, our analysis of Eq. (10) has considered the case of zero damping ($\zeta = 0$). To gain a better understanding of the full oscillator dynamics, we now present numerical bifurcation results for the system with nonzero damping and with the detuning (σ) treated as a bifurcation parameter. These results are obtained using AUTO [23], which requires that we rewrite the non-autonomous Eq. (10) as a system of autonomous first-order equations. Rewriting this as first-order equations is accomplished by defining $v = z'$ and considering equations for z' and v' . We make this system autonomous by augmenting Eq. (10) with equations for a nonlinear oscillator with a stable periodic orbit with one variable equal to $\cos \Omega \tau$, and replacing the appropriate terms of Eq. (10) with this variable. Most of our attention will be on Region IV from Fig. 2, as this displays the most interesting bifurcation behavior. We will also present typical results for Regions I Ib, III, and Va; Regions I, IIa, Vb, and VI are related to the presented regions by symmetry.

As a typical point in Region IV, we take $\lambda_1 = \nu_1 = 1$ and $\gamma_3 = \lambda_3 = -0.005$, as in Fig. 7. Throughout this section, we take $\varepsilon = 0.1$. The no-motion state ($z = z' = 0$) exists for all values of ζ and σ , and undergoes bifurcations giving rise to branches of periodic orbits which may be followed with AUTO. These periodic orbits display response at half the driving frequency Ω , and have the symmetry property

$$(z, z')(\tau + T/2) = (-z, -z')(\tau), \quad (48)$$

where $T = 2\pi/\Omega$ is the period of the response. Already for small damping we find the interesting result that the constant amplitude branch shown in Fig. 7 splits such that the branches with the distinct phases now have slightly different amplitudes; see Fig. 20 for results with $\zeta = 0.001$. Here the stable periodic orbit branch which bifurcates from the trivial solution at $\sigma \approx 1.5$ undergoes a saddle-node bifurcation at $\sigma \approx -1$ before returning to the trivial state in the bifurcation at $\sigma \approx 0.5$. The branch containing the stable periodic orbit for $\sigma = -1$ undergoes a saddle-node bifurcation at $\sigma \approx 0$, and is disconnected from the no-motion state. Periodic orbits on this disconnected branch also display the symmetry given in Eq. (48).

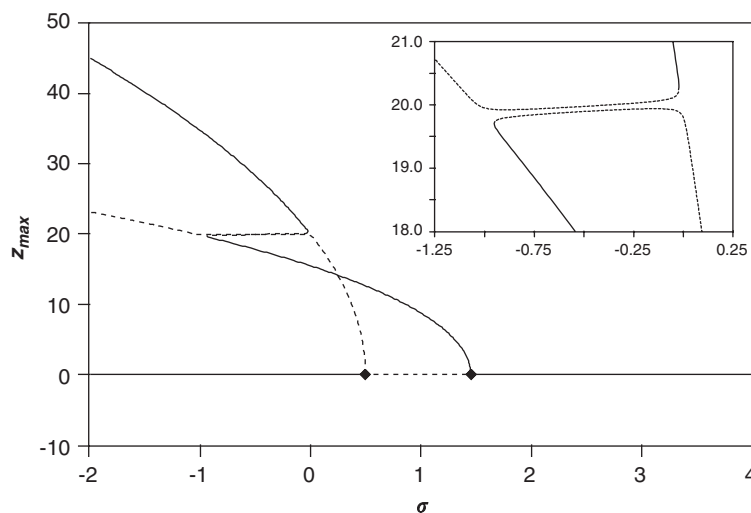


Fig. 20. Bifurcation diagram showing the maximum value of the displacement (z_{\max}) for $\zeta = 0.001$ and other parameters as described in the text. In this and other bifurcation diagrams, diamonds, squares, and triangles indicate crossing the boundary of an Arnold tongue, period-doubling, and symmetry-breaking pitchfork bifurcations, respectively. Furthermore, solid and dashed lines represent stable and unstable solutions, respectively.

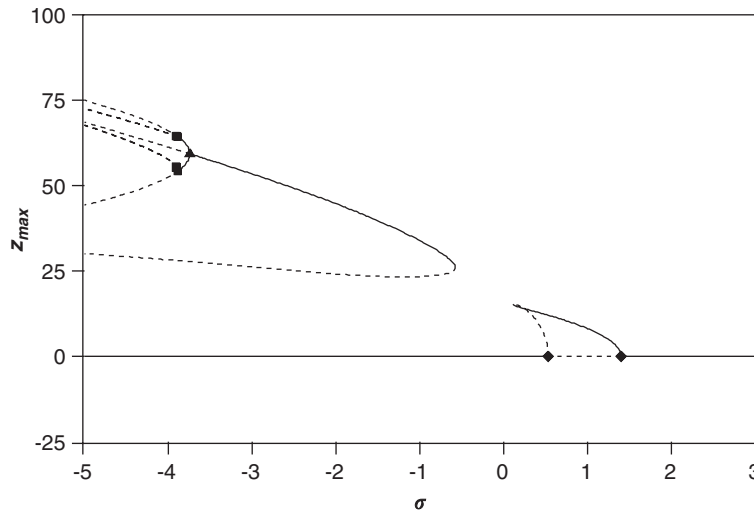


Fig. 21. Bifurcation diagram for $\zeta = 0.1$ and other parameters corresponding to Region IV, as described in the text.

For larger damping, we find additional bifurcations on the disconnected branch; see Fig. 21 for $\zeta = 0.1$ (a very large value for a MEM resonator). A periodic orbit with the symmetry of Eq. (48) is stable from $-0.570 < \sigma < -3.739$; a typical orbit is shown in Fig. 22(a). At the upper limit it undergoes a saddle-node bifurcation, while at the lower limit it undergoes a symmetry-breaking pitchfork bifurcation. The symmetry-breaking bifurcation leads to two symmetry-related asymmetric periodic orbits, which lack the symmetry given in Eq. (48); see Fig. 22(b) for an example of one of these (the other is obtained by letting $(z, z') \rightarrow (-z, -z')$). Each of these symmetry-related asymmetric periodic orbits undergoes a period-doubling bifurcation at $\sigma = -3.884$; one of the period-doubled orbits is shown in Fig. 22(c). This is the beginning of a period-doubling cascade to chaos as σ decreases, with chaotic attractor as shown in Fig. 22(d). This is one of two symmetry-related chaotic attractors (the other is obtained by letting $(z, z') \rightarrow (-z, -z')$). We note that the basin of attraction for this chaotic attractor is quite small, making it somewhat difficult to locate (and likely unobservable in physical experiments). We also note that from [24], it is necessary for a symmetric periodic orbit such as that shown in Fig. 22(a) to first undergo a symmetry-breaking bifurcation before a period-doubling cascade can occur.

Fig. 23 shows results from a two-parameter (σ and ζ) bifurcation study for the Region IV parameters used above. The no-motion state is unstable inside the dashed curve. The width of this instability region decreases as the damping ζ increases, consistent with the effect of damping for the related Mathieu equation [21]. The dot-dashed lines show bifurcation sets for the saddle-node bifurcations of the symmetric periodic orbits. The crossing of these at $(\sigma, \zeta) \approx (-0.3, 0.05)$ does not correspond to a codimension-two bifurcation; the two saddle-node bifurcations are just (independently) occurring at the same parameter values. One dash-dotted curve (corresponding to a saddle-node bifurcation of the periodic orbit branch which bifurcates from the no-motion branch) terminates on the dashed curve at $(\sigma, \zeta) \approx (0.796, 0.222)$. Here the periodic orbit branch emerging from the no-motion branch bifurcates vertically. For smaller ζ values, there is an unstable periodic orbit bifurcating to smaller σ values (which then turns around in a saddle-node bifurcation), while for larger ζ values there is a stable branch which bifurcates to larger σ values.

We now consider the point in Region Va with $\lambda_1 = \nu_1 = 1$ and $\gamma_3 = -0.005, \lambda_3 = -0.01$, as in Fig. 9. For small ζ we similarly find that the constant amplitude solution branch shown in Fig. 9 splits, giving a periodic orbit branch which is disconnected from the no-motion state; see Fig. 24 for $\zeta = 0.001$. This disconnected branch persists for larger ζ ; see Fig. 25 for $\zeta = 0.1$, for which we do not find any further bifurcations. Note that we obtained unstable periodic orbits on the disconnected branch using a shooting method, and these were then followed with AUTO.

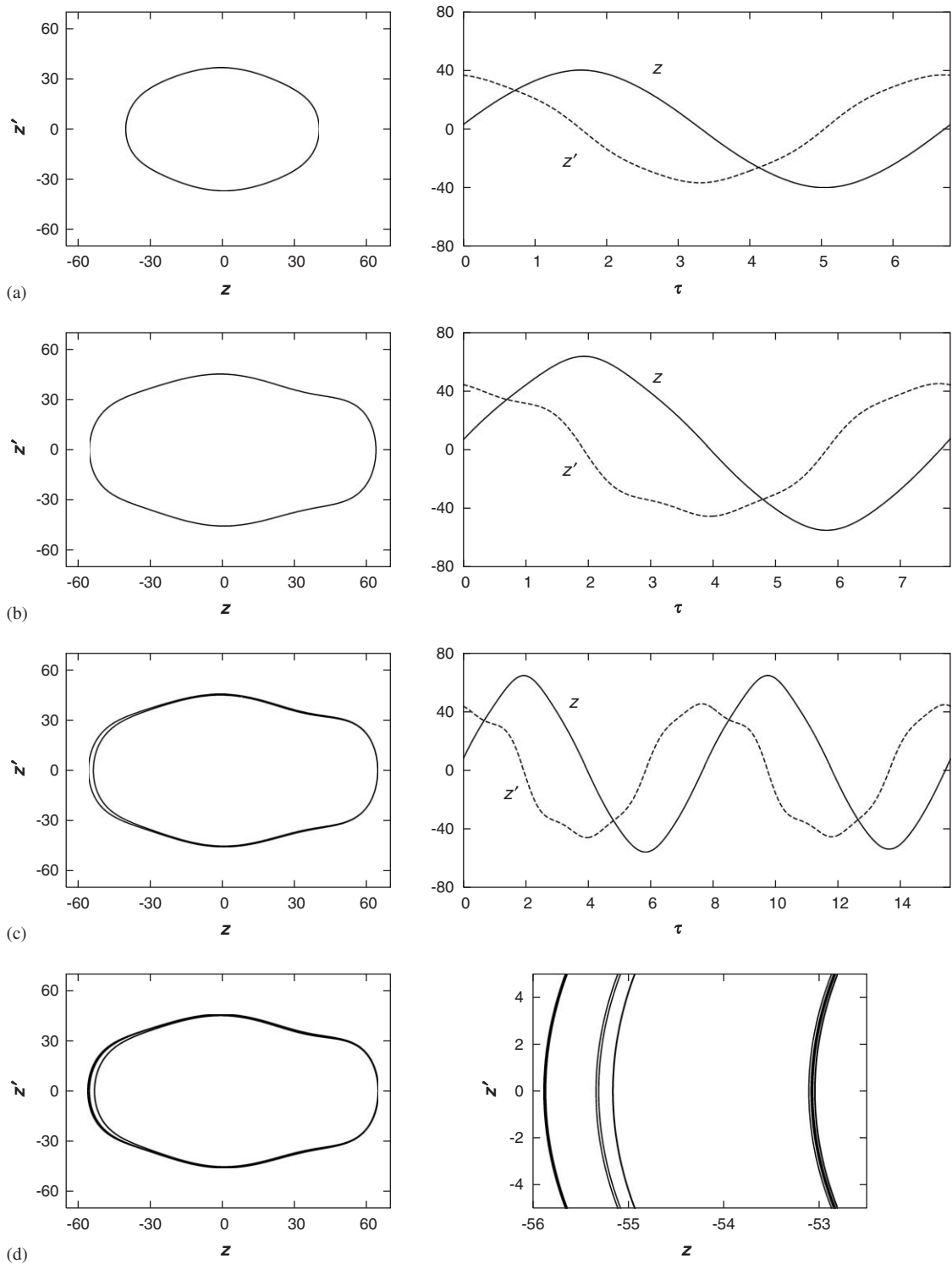


Fig. 22. Stable solutions for parameters as in Fig. 21 and with forcing $\sim \cos \Omega t$: (a) symmetric periodic orbit for $\sigma = -1.5$; (b) asymmetric periodic orbit for $\sigma = -3.85$; (c) period doubled orbit for $\sigma = -3.895$; (d) chaotic solution for $\sigma = -3.90235$, with right panel zoomed in. The timeseries in (a), (b), and (c) show one period.

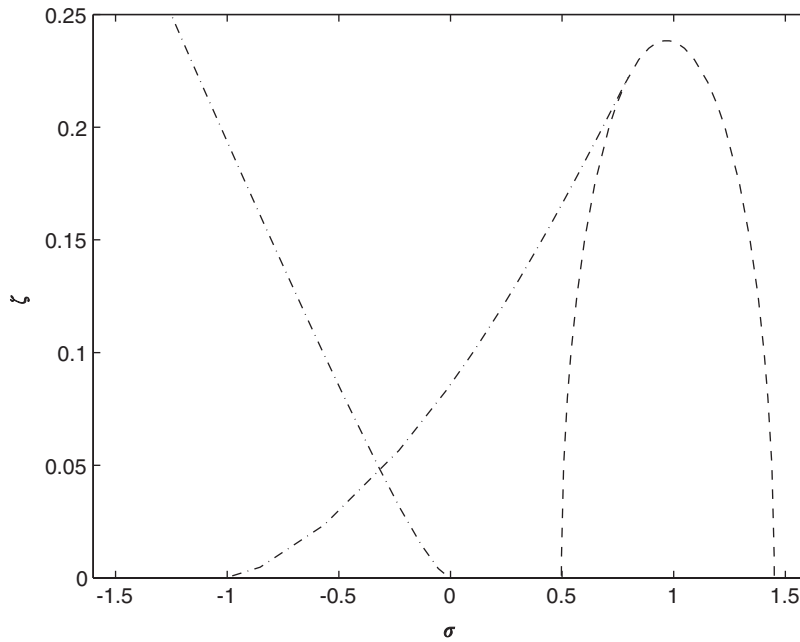


Fig. 23. Bifurcation sets for the parameters corresponding to Region IV. The no-motion state is unstable inside the dashed curve, while the dot-dashed lines show bifurcation sets for the saddle-node bifurcations of the symmetric periodic orbits.

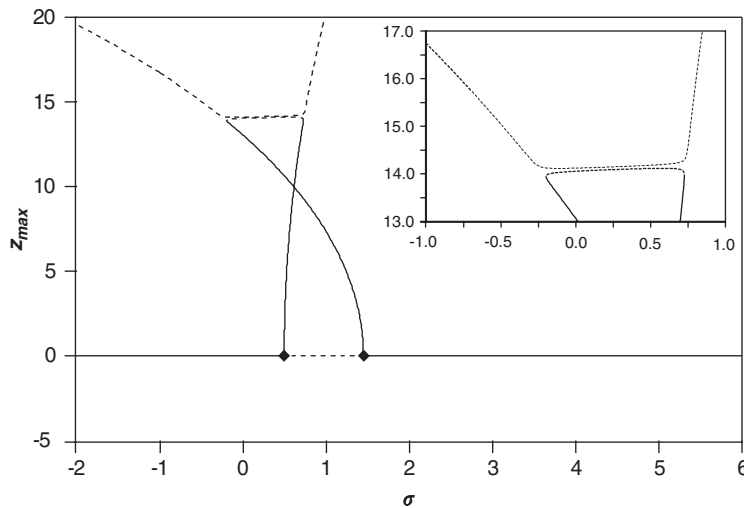


Fig. 24. Bifurcation diagram for $\zeta = 0.001$ and other parameters corresponding to Region Va, as described in the text.

A similar period-doubling cascade to chaos, as found above for Region IV, is present for $\zeta = 0.1$ for the point in Region III with $\lambda_1 = \nu_1 = 1$ and $\gamma_3 = -0.005, \lambda_3 = 0.005$, as in Fig. 6; see Fig. 26. In this region, there are no constant amplitude solutions for $\zeta = 0$, as there were for Region IV.

We close this section by noting that no interesting bifurcation behavior is found for $\zeta = 0.1$ for the point in Region IIb with $\lambda_1 = \nu_1 = 1$ and $\gamma_3 = -0.005, \lambda_3 = 0.01$, as in Fig. 5.

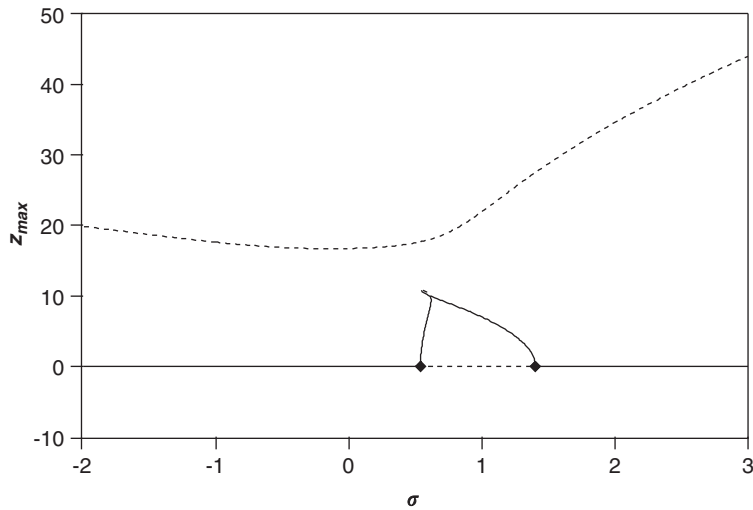


Fig. 25. Bifurcation diagram for $\zeta = 0.1$ and other parameters corresponding to Region Va, as described in the text.

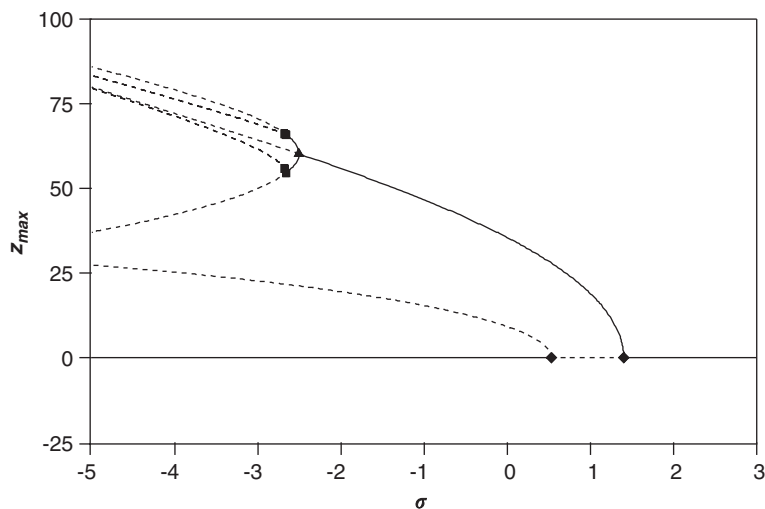


Fig. 26. Bifurcation diagram for $\zeta = 0.1$ and other parameters corresponding to Region III, as described in the text.

7. Application to MEM resonators

The results developed in the previous sections are directly applicable to the equations of motion for parametrically excited MEM oscillators of the type developed in Section 2. However, in this case, the coefficients in the equation of motion that are related to the electrostatic forces depend on the amplitude of the AC voltage, V_A . Accordingly, the qualitative nature of both the linear and nonlinear behavior of the oscillator depend on V_A .

The effect of varying V_A on the linear behavior of the system is easily noted by considering the undamped MEM oscillator's linear stability chart, as presented in Fig. 27. As clearly shown, as V_A is increased, the width (in terms of detuning) of the linear instability zone increases. As noted in Section 4, this is largely consistent

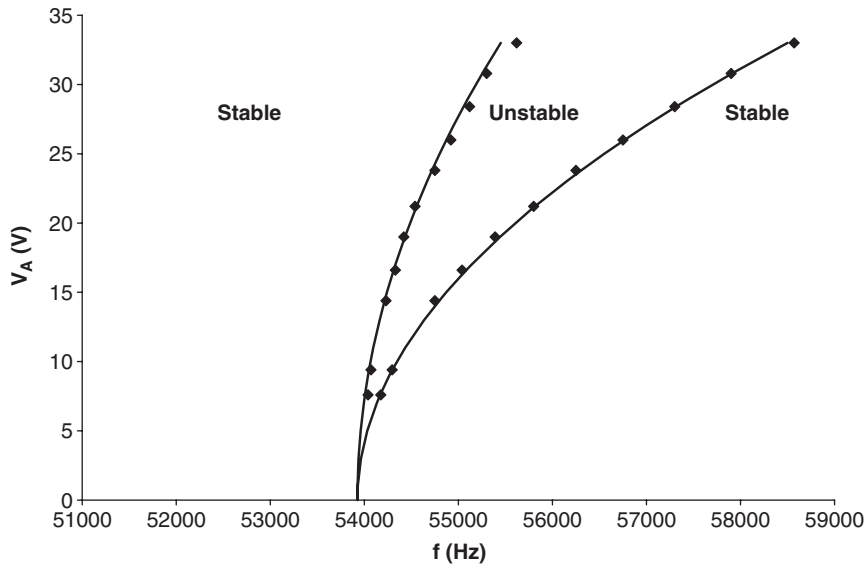


Fig. 27. Linear stability chart in the AC excitation voltage amplitude (V_A) versus excitation frequency (f) parameter space for an undamped MEM oscillator with system parameters as specified in Table 2. Experimentally derived instability points are also shown. Note that in each case the noted stability corresponds to the trivial solution.

with the behavior of a typical Mathieu system, but with two notable exceptions. First, due to the nonlinear relationship between λ_1 and V_A the boundaries of the instability feature a distinct curvature. In addition, due to the presence of the frequency shift caused by the electrostatic stiffness term (λ_1), the instability region is distorted from its nominally symmetric configuration. Each of these differences is examined extensively in Ref. [1]. From a practical point of view, it is also important to note that in the presence of damping, the bottom of the instability wedge in Fig. 27 pulls up from zero voltage and becomes rounded off, as shown experimentally in both Fig. 27 and Ref. [15].

The effect of V_A on the nonlinear behavior of the system can be realized by noting that as the excitation amplitude is varied, the system can transition from one response regime to another (in Fig. 2). This can be confirmed by examining the form of the nonlinearity in the γ_3 – λ_3 parameter space. Taking the definitions of λ_3 and γ_3 from Table 1 it is seen that at zero voltage the system starts at $(\gamma_3, \lambda_3) = (\chi, 0)$ (the point corresponding to the purely mechanical hardening nonlinearity), which lies on the boundary between Regions I and VI, and moves along a straight line in the γ_3 – λ_3 parameter space given by

$$\lambda_3 = \gamma_3 - \chi \tag{49}$$

as V_A is increased [1,5]. To validate this, consider the oscillator design described by the parameters in Table 2, which were obtained, as subsequently described, from a device similar to that shown in Fig. 1. As Fig. 28 shows, the nonlinearity for this device will move through regions VI, Vb, Va, and IV as the amplitude of the AC voltage is varied. Thus, the system transitions from a quasi-hardening nonlinearity, to a mixed nonlinearity, and finally to a quasi-softening nonlinearity as the oscillator’s input voltage increases. Figs. 29–31 show response curves for the experimental parameter values for three different values of V_A . Note that the response indeed transitions from hardening, to mixed, to softening, as predicted.

With the aforementioned behavior in mind, a designer can account for these transitions and estimate whether or not they will occur in a given device’s operating voltage range. The following relationships, derived by setting η_1 and η_2 equal to zero, provide expressions for the transition voltages, that is, the critical voltage values corresponding to qualitative changes in the system’s nonlinearity. For a given oscillator,

$$V_{A,C1} = \sqrt{\frac{-3k_3}{5r_{3A}}} \tag{50}$$

Table 2
Design parameters for a representative MEM oscillator

Parameter	Value
$r_{1,A}$	$2.96 \times 10^{-4} \mu\text{N}/\text{V}^2 \mu\text{m}$
$r_{3,A}$	$-2.1 \times 10^{-4} \mu\text{N}/\text{V}^2 \mu\text{m}^3$
k_1	$2.85 \mu\text{N}/\mu\text{m}$
k_3	$0.075 \mu\text{N}/\mu\text{m}^3$
c	$3.88 \times 10^{-8} \text{kg/s}$
m	$9.93 \times 10^{-11} \text{kg}$

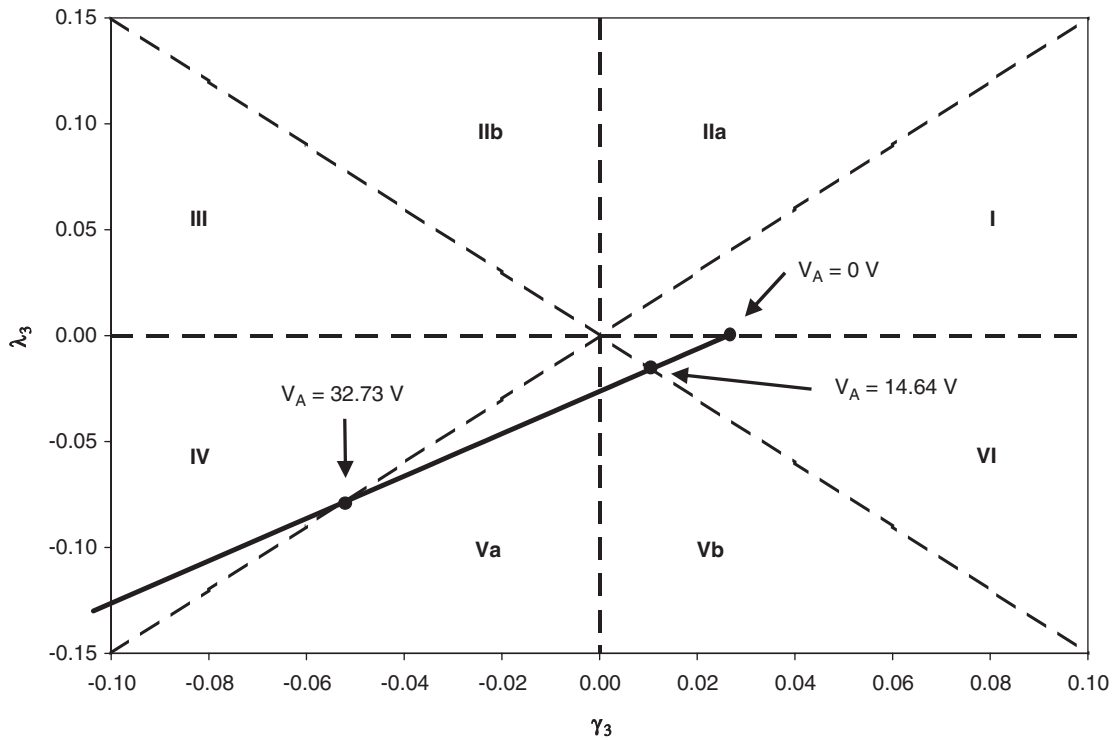


Fig. 28. Sample nonlinear parameter space showing how the system nonlinearity transitions between response regimes under a varying AC voltage amplitude for the device presented in Table 2.

represents the voltage at which $\eta_2 = 0$, and

$$V_{A,C2} = \sqrt{\frac{-3k_3}{r_{3,A}}}, \quad (51)$$

represents the voltage at which $\eta_1 = 0$. For the device under consideration, these voltages are predicted to be 14.64 and 32.73 V, respectively.

For the sake of reference, it also proves convenient to address the MEM oscillator's linear and nonlinear behavior in the context of a bifurcation diagram, in this case in terms of the oscillator's voltage excitation amplitude versus excitation frequency parameter space, as shown in Fig. 32. This plot not only confirms the aforementioned assertions pertaining to the system's Arnold tongue, especially with regard to the effects of damping, but also identifies the location of the saddle-node bifurcations of principal interest, namely those

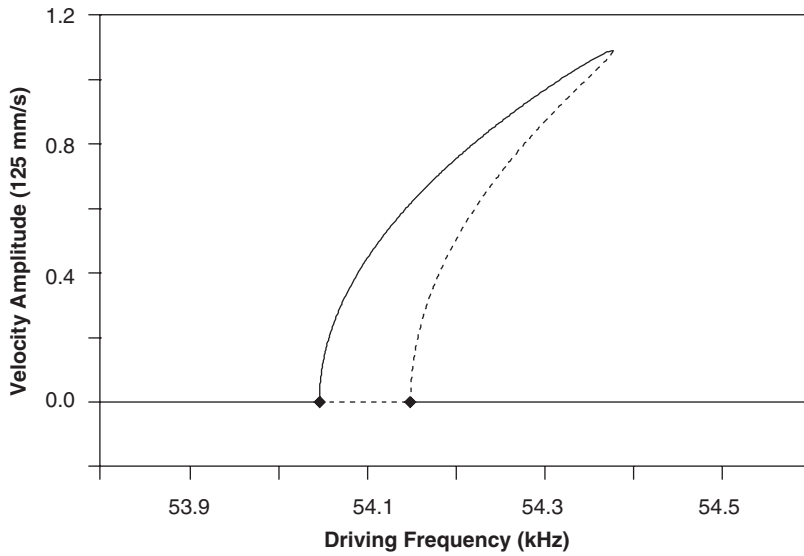


Fig. 29. Numerical frequency response curves for $V_A = 7.6$ V. Note the hardening behavior exhibited in the system’s frequency response.

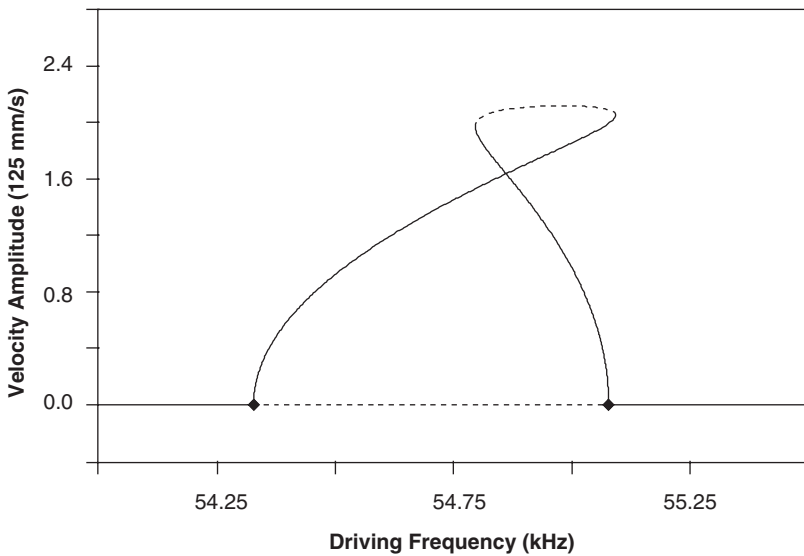


Fig. 30. Numerical frequency response curves for $V_A = 16.6$ V. Note the mixed nonlinear behavior exhibited in the system’s frequency response.

which correspond to a stability change in the nontrivial stable response branches emanating from $a = 0$, and the effect of damping on their locations.² Of particular note here is the distortion of the saddle-node bifurcations produced by small damping. In particular, small damping destroys the excitation amplitude independence of one saddle-node branch and shifts each of their locations. However, from a practical point of

²Though other saddle-node curves exist, they are omitted here since they involve stable isolated or unstable response branches, and are thus not present in the experimental results presented subsequently.

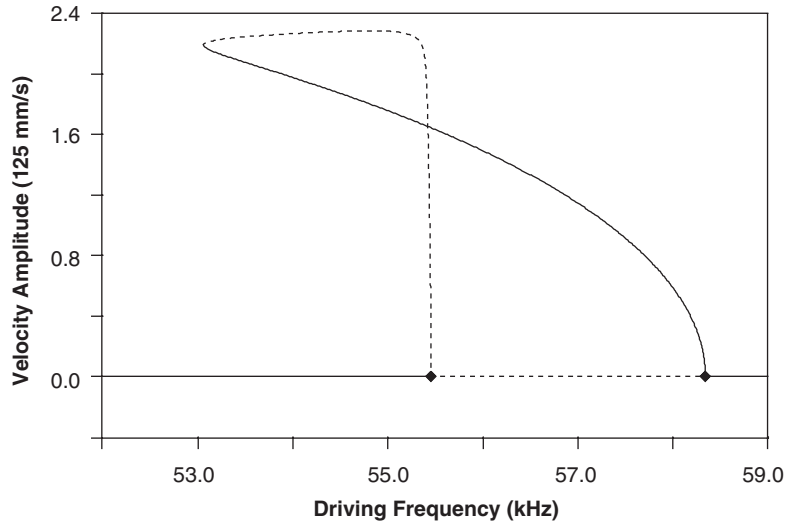


Fig. 31. Numerical frequency response curves for $V_A = 33.0$ V. Note the softening (quasi-softening) behavior exhibited in the system’s frequency response.

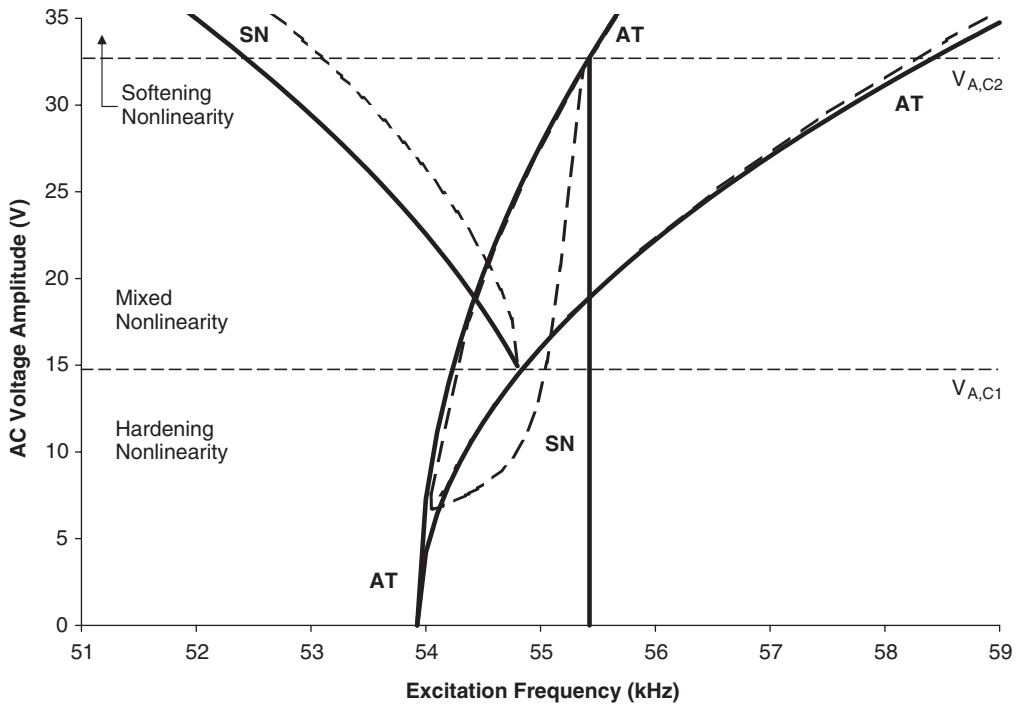


Fig. 32. Bifurcation diagram created using both analytical and numerical techniques. Note that the solid curves were produced using analytical results obtained for the undamped system ($\zeta = 0$). The dashed lines ($\zeta \approx 0.001$) were produced using results obtained numerically using AUTO for an analogous system with small damping. Note that the lines labeled AT correspond to the bifurcations associated with the Arnold tongue and those labeled SN correspond to saddle-node bifurcations.

view, this is of minimal concern as the transition voltages appear to be largely invariant with respect to small damping and thus predictive design of the oscillators is largely uninhibited by such concerns (though this, as subsequently shown, could have an effect on the accuracy of parameter identification).

In order to confirm the general behavior predicted by this analysis, some previously obtained experimental results from a MEM oscillator are included in Figs. 33–35. These figures depict frequency response curves of velocity amplitude versus AC voltage frequency for the device in question at AC voltage excitation amplitudes

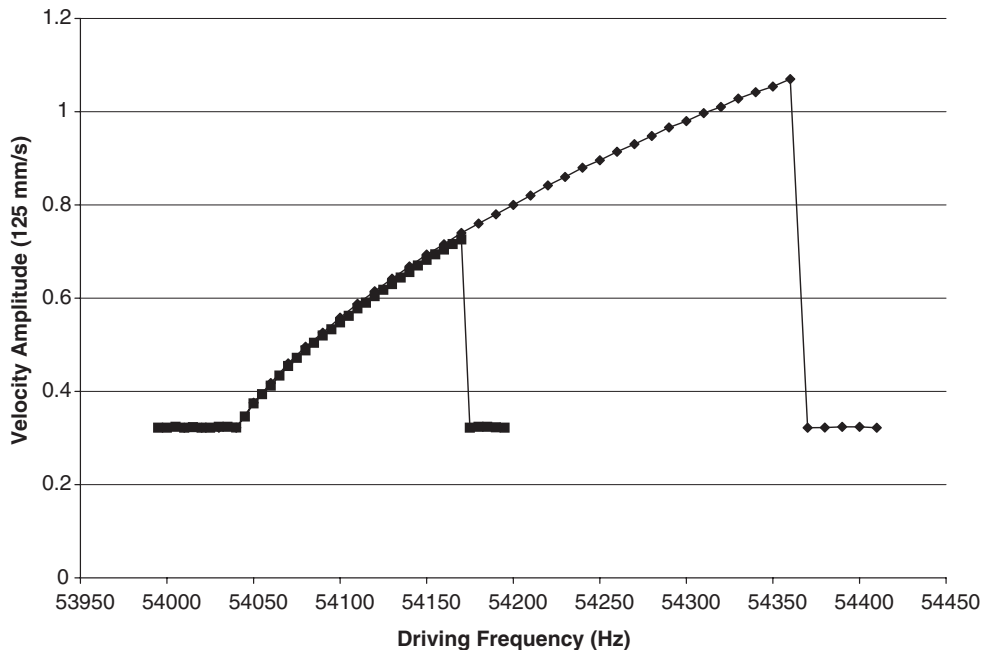


Fig. 33. Experimental frequency response curves for $V_A = 7.6$ V. Diamonds correspond to the up sweep data points and squares to the down sweep data points. Note the hardening behavior exhibited in the system's frequency response.

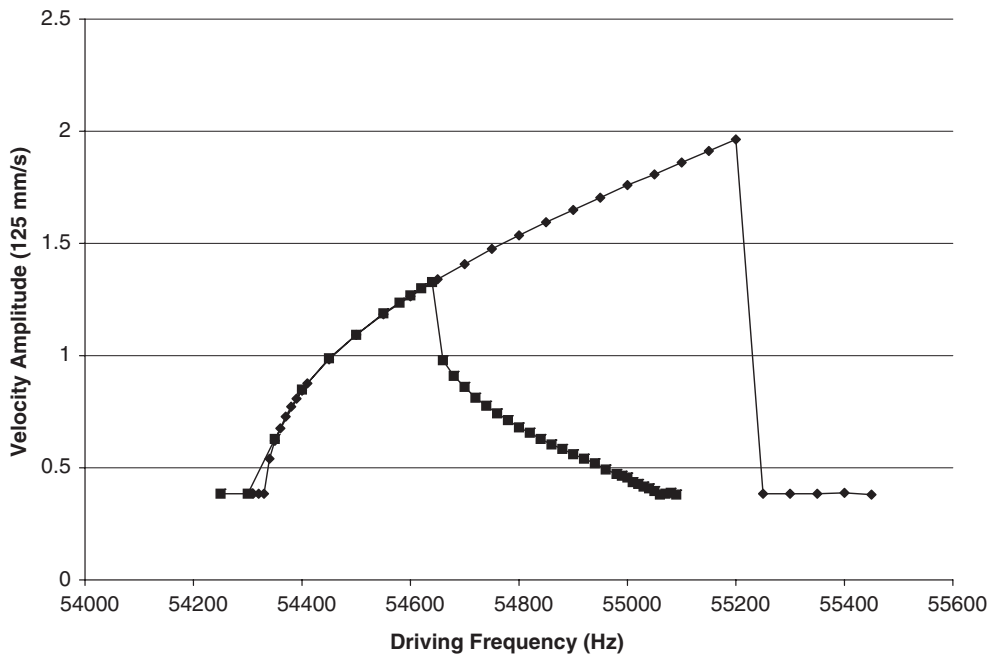


Fig. 34. Experimental frequency response curves for $V_A = 16.6$ V. Diamonds correspond to the up sweep data points and squares to the down sweep data points. Note the mixed non-linear behavior exhibited in the system's frequency response.

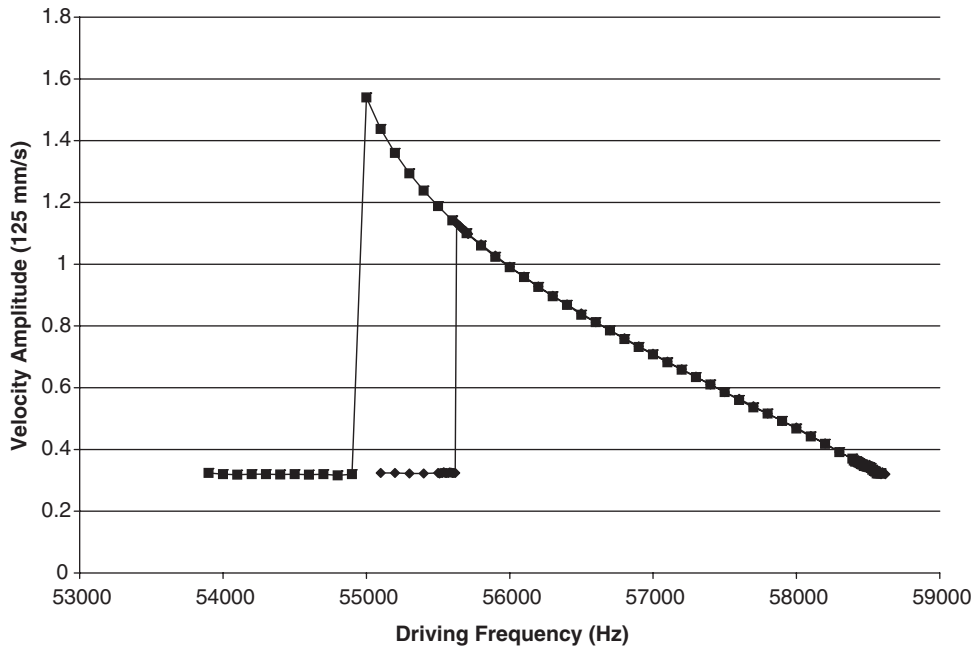


Fig. 35. Experimental frequency response curves for $V_A = 33.0$ V. Diamonds correspond to the up sweep data points and squares to the down sweep data points. Note the softening behavior exhibited in the system's frequency response.

(V_A) of 7.6, 16.6, and 33.0 V, respectively (the same values as used for the simulated results). As predicted, the oscillator's nonlinear characteristics qualitatively change as the excitation voltage is increased. Specifically, the oscillator exhibits hardening characteristics at 7.6 V, mixed nonlinear characteristics at 16.6 V, and softening characteristics at 33.0 V, in complete qualitative agreement with the simulation results.

It is important to note that the quantitative compatibility of the simulation and experimental results presented is based on the fact that the set of experiments that generated Figs. 33–35 were used for parameter identification (further details of which can be found in Ref. [25]). Specifically, the experimentally identified bifurcation points associated with crossing the Arnold tongue were compared with numerical simulations to determine, via a nonlinear least-squares fit, the linear system parameters (r_{1A} , k_1 , c , and m) and the experimentally identified saddle-node bifurcations associated with the periodic orbits were compared (visually) to numerical simulations and the analytically derived transition voltages to determine the nonlinear system parameters (r_{3A} and k_3). Though this identification process was partially done in an ad hoc manner (systematically, but in certain cases visually), the results are quite promising and, from a parameter perspective, in general agreement with approximations produced via finite element techniques. In fact, a quite complete comparison of the predicted and measured bifurcation sets is given in Fig. 36. It is seen that the Arnold tongue and the higher frequency saddle-node bifurcations are well predicted, but that the model does not accurately capture the frequencies at which the lower-frequency saddle-node occurs. However, it should be noted that the model does a very good job at predicting the ranges of V_A over which hardening, mixed, and softening nonlinear behaviors are observed.

While the experimental results presented are promising indications of the validity of the analysis presented, some issues remain to be resolved. For example, the absence of effects associated with the additional constant amplitude solution is slightly disconcerting. This, however, is largely reconcilable with the fact that the authors were not aware of such phenomena previous to and during the experimentation which produced the included results, and thus this phenomena was not taken into account during frequency sweeps and device characterization. In addition, the parameter identification technique used to determine the parameters presented in Table 2 could undergo refinement. For example, robust nonlinear curve-fitting techniques could be used in place of the visual approach employed here. Each of these issues and others, such as the discrepancy

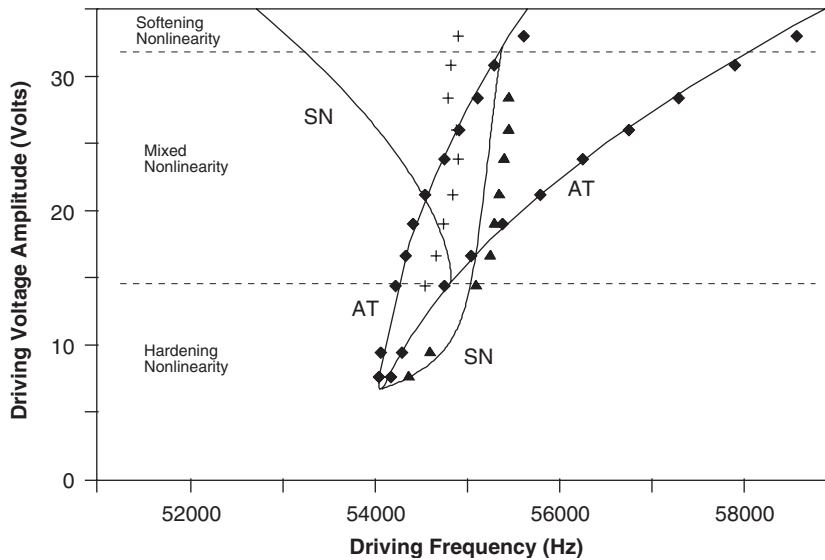


Fig. 36. The voltage amplitude versus excitation frequency parameter space which was used to recover the system parameters presented in Table 2. The solid lines designated AT and SN correspond to the numerically predicted location of the Arnold tongue and saddle-node bifurcations, respectively. The various data points, which were determined experimentally, correspond to the Arnold tongue (diamonds), left saddle-node bifurcation (crosses), and right saddle-node bifurcation (triangles). Note the strong correlation produced by the parameter identification process.

between numerically predicted and experimentally determined response amplitudes and parameter sensitivity, will be addressed in forthcoming works.

8. Conclusion

As shown in this work, parametrically excited MEM oscillators and other systems with generalized forms of parametric resonance can exhibit a wide array of interesting dynamical behavior, most of which can be attributed to the existence of nonlinear parametric excitation in their respective equations of motion. One interesting result of this nonlinear parametric excitation is that such systems fail to exhibit a single effective nonlinearity that is capable of characterizing their nonlinear behavior (in terms of frequency response). Instead, the systems feature multiple effective nonlinearities, which only when collectively analyzed reveal their nonlinear nature. Accordingly, such systems are capable of displaying not only typical hardening or softening nonlinear characteristics, but also mixed nonlinear characteristics wherein the principal response branches bend toward or away from one another near resonance. In fact, for certain devices, perhaps most notably parametrically excited MEM oscillators, such behavior can be shown to be explicitly dependent on the excitation amplitude of the system. That is, such systems can be shown to transition between various qualitatively different nonlinear regimes as the excitation amplitude is varied.

Experimentation has yielded results that are in good agreement with the analytical predictions developed. In particular, experimentally produced frequency response and bifurcation diagrams confirm the assertion that the qualitative nature of the systems' nonlinear response can change with the systems' excitation amplitude.

Despite the general agreement between the analytical, numerical, and experimental results presented in this work, some issues remain unresolved. As highlighted in the previous section, these issues include the experimental identification of effects associated with the constant amplitude solutions, which should give rise to isolated response branches, and improvement in parameter estimation techniques. Both of these issues, as well as others, including the possible need to include higher-order nonlinearities in the system model, are

currently being addressed through an experimental campaign designed to systematically characterize such systems in light of the analytical and numerical results presented in this work.

In terms of device design, it is often desirable to have a system that is either purely hardening, or purely softening. It is relatively simple to achieve overall hardening behavior, since virtually all mechanical suspensions lead to hardening nonlinearities. Thus, one can design comb drives that will maintain the system in Region I or VI as V_A is varied. The case of softening nonlinearity is more complicated, since no known mechanical suspension leads to softening behavior. In this case, the suspension should be made as linear as possible, and the comb drive designed so that the system transitions from Region VI through Regions Va and Vb at very low voltages, resulting in a system that is softening beyond a low threshold. This is not problematic, however, since the applied voltage must be above a certain threshold in order to activate the parametric resonance (due to the presence of damping).

The results presented are directly applicable to other microscale systems, such as electrostatically actuated microbeams and torsional oscillators, and are also extendable to a variety of systems on the macroscale. It is hoped that the general response features and predictive tools described herein are beneficial in the design and evaluation of these systems.

Acknowledgments

This work was supported by the Air Force Office of Scientific Research (AFOSR) under contract F49620-02-1-0069 and by the National Science Foundation under Grant NSF-0428916.

References

- [1] J.F. Rhoads, S.W. Shaw, K.L. Turner, R. Baskaran, Tunable MEMS filters that exploit parametric resonance, *ASME Journal of Vibration and Acoustics* 127 (5) (2005) 423–430.
- [2] W. Zhang, R. Baskaran, K.L. Turner, Tuning the dynamic behavior of parametric resonance in a micromechanical oscillator, *Applied Physics Letters* 82 (1) (2003) 130–132.
- [3] W. Zhang, R. Baskaran, K.L. Turner, Effect of cubic nonlinearity on auto-parametrically amplified resonant MEMS mass sensor, *Sensors and Actuators A: Physical* 102 (1–2) (2002) 139–150.
- [4] W. Zhang, K. Turner, A mass sensor based on parametric resonance, *Proceedings of the Workshop on Solid-State Sensors and Actuators*, Hilton Head, South Carolina, 2004, 49–52.
- [5] J.F. Rhoads, Parametrically-excited Microelectromechanical Oscillators with Filtering Capabilities, MS Thesis, Michigan State University, 2004.
- [6] S.W. Shaw, K.L. Turner, J.F. Rhoads, R. Baskaran, Parametrically excited MEMS-based filters, *Proceedings of the IUTAM Symposium on Chaotic Dynamics and Control of Systems and Processes*, 2003, 137–146.
- [7] K.B. Lee, Y.-H. Cho, Electrostatic control of mechanical quality factors for surface-micromachined lateral resonators, *Journal of Micromechanics and Microengineering* 6 (4) (1996) 426–430.
- [8] L. Lin, R.T. Howe, A.P. Pisano, Microelectromechanical filters for signal processing, *Journal of Microelectromechanical Systems* 7 (3) (1998) 286–294.
- [9] W.C. Tang, T.-C.H. Nguyen, R.T. Howe, Laterally driven polysilicon resonant microstructures, *Sensors and Actuators* 20 (1989) 25–32.
- [10] W. Ye, X. Wang, W. Hemmert, D. Freeman, J. White, Air damping in laterally oscillating microresonators: a numerical and experimental study, *Journal of Microelectromechanical Systems* 12 (5) (2003) 557–566.
- [11] G.T. Abraham, A. Chatterjee, Approximate asymptotics for a nonlinear Mathieu equation using harmonic balance based averaging, *Nonlinear Dynamics* 31 (2003) 347–365.
- [12] M. Mond, G. Cederbaum, P.B. Khan, Y. Zarmi, Stability analysis of the non-linear Mathieu equation, *Journal of Sound and Vibration* 167 (1) (1993) 77–89.
- [13] D. Younesian, E. Esmailzadeh, R. Sedaghati, Existence of periodic solutions for the generalized form of Mathieu equation, *Nonlinear Dynamics* 39 (4) (2004) 335–348.
- [14] W. Zhang, R. Baskaran, K.L. Turner, Changing the behavior of parametric resonance in MEMS oscillators by tuning the effective cubic stiffness, *Proceedings of the 16th Annual International Conference on Micro Electro Mechanical Systems*, IEEE, Kyoto, Japan, 2003, pp. 173–176.
- [15] K.L. Turner, S.A. Miller, P.G. Hartwell, N.C. MacDonald, S.H. Strogatz, S.G. Adams, Five parametric resonances in a microelectromechanical system, *Nature* 396 (1998) 149–152.
- [16] W. Zhang, R. Baskaran, K.L. Turner, Nonlinear dynamics analysis of a parametrically resonant MEMS sensor, *Proceedings of the 2002 SEM Annual Conference and Exposition on Experimental and Applied Mechanics*, Milwaukee, Wisconsin, 2002.

- [17] S. Natsiavas, S. Theodossiades, I. Goudas, Dynamic analysis of piecewise linear oscillators with time periodic coefficients, *International Journal of Non-Linear Mechanics* 35 (1) (2000) 53–68.
- [18] S. Theodossiades, S. Natsiavas, Non-linear dynamics of gear-pair systems with periodic stiffness and backlash, *Journal of Sound and Vibration* 229 (2) (2000) 287–310.
- [19] J.A. Sanders, F. Verhulst, *Averaging Methods in Nonlinear Dynamical Systems, Applied Mathematical Sciences*, Vol. 59. Springer, New York, 1985.
- [20] S.H. Strogatz, *Nonlinear Dynamics and Chaos with Applications to Physics, Biology, Chemistry and Engineering*, Westview, Cambridge, 1994.
- [21] A.H. Nayfeh, D.T. Mook, *Nonlinear Oscillations*, Wiley-Interscience, New York, 1979.
- [22] J.J. Stoker, *Nonlinear Vibrations in Mechanical and Electrical Systems*, Wiley, New York, 1950.
- [23] E. Doedel, A. Champneys, T. Fairgrieve, Y. Kuznetsov, B. Sandstede, X. Wang, *AUTO 97: Continuation and Bifurcation Software for Ordinary Differential Equations*, 1997.
- [24] J.W. Swift, K. Wiesenfeld, Suppression of period doubling in symmetric systems, *Physical Review Letters* 52 (1984) 705–708.
- [25] B. DeMartini, J. Moehlis, K. Turner, J. Rhoads, S. Shaw, W. Zhang, Modeling of parametrically excited microelectromechanical oscillator dynamics with application to filtering, *Proceedings of the Fourth IEEE Conference on Sensors (IEEE Sensors 2005)*, 2005, 345–348.